1 **Regular Article**

2

3 ***TET2*-mutant clonal hematopoiesis prevents T-cell exhaustion and suppresses cancer**
4 **metastasis**

5

6 Ai Nhan Thi Le[1], Manabu Fujisawa[2,3], Giacomo Campo[4], Yen T M Nguyen[2], Tran Bich
7 Nguyen[2], Sakurako Suma[2, 5], Yasuhito Suehara[2, 5], Fumihito Miura[6], Hiromitsu Araki[7],
8 Kenichi Makishima[2, 5], Tatsuhiro Sakamoto[2, 5], Mizuho Nakayama[8, 9], Masanobu Oshima[8, 9],
9 Miwako Kakiuchi[10], Shumpei Ishikawa[10], Chizu Tanikawa[11], Koichi Matsuda[11], Ryunosuke
10 Saiki[12, 13], Seishi Ogawa[12, 13], MVanner, Robert J.[4,14]*, and Mamiko Sakata-Yanagimoto[2,5,15]*

11

12 *1 Department of Hematology, Graduate School of Comprehensive Human Sciences, University of*
13 *Tsukuba, Tsukuba, Japan.*
14 *2 Department of Hematology, Institute of Medicine, University of Tsukuba, Tsukuba, Japan.*
15 *3 Centre for Lymphoid Cancer, BC Cancer, Vancouver, BC, Canada.*
16 *4 Division of Medical Oncology and Hematology, Princess Margaret Cancer Centre, University*
17 *Health Network, Toronto, Canada*
18 *5 Department of Hematology, University of Tsukuba Hospital, Tsukuba, Japan.*
19 *6 Graduate School of Frontier Sciences, the University of Tokyo, Kashiwa, Japan.*
20 *7 Medical Institute of Bioregulation, Kyushu University, Fukuoka, Japan.*
21 *8 Division of Genetics, Cancer Research Institute, Kanazawa University, Kanazawa, Japan.*
22 *9 WPI Nano Life Science Institute, Kanazawa University, Kanazawa, Japan.*

10 Department of Preventive Medicine, Graduate School of Medicine, The University of Tokyo, Tokyo, Japan.

11 Laboratory of Clinical Genome Sequencing, Graduate School of Frontier Sciences, The University of Tokyo, Tokyo, Japan.

12 Department of Pathology and Tumor Biology, Graduate School of Medicine, Kyoto University, Kyoto, Japan.

13 Institute for the Advanced Study of Human Biology (WPI ASHBi), Kyoto University, Kyoto, Japan.

14 Institute of Medical Science, Temerty Faculty of Medicine, University of Toronto, Toronto, Canada.

15 Division of Advanced Hemato-Oncology, Transborder Medical Research Center, University of Tsukuba, Tsukuba, Japan.

***Correspondence:**

Mamiko Sakata-Yanagimoto, MD, PhD

Department of Hematology, Institute of Medicine, University of Tsukuba.

1-1-1 Tennodai, Tsukuba, Ibaraki 305-8575, Japan

TEL +81-29-853-3127, FAX +81-29-853-8079, E-mail: sakatama@md.tsukuba.ac.jp

and Robert J. Vanner, MD, PhD

Division of Medical Oncology and Hematology, Princess Margaret Cancer Centre, University Health Network.

610 University Ave, Toronto, ON, Canada, M5G 2C4

TEL +1-416-946-4501x8673, FAX +1-416-946-6546, E-mail: robert.vanner@uhn.ca

ABSTRACT

Clonal hematopoiesis (CH) is widely regarded as a risk factor for age-associated disease, yet its influence on solid tumor progression remains poorly understood. Here, we uncover an unexpected tumor-suppressive role for *TET2*-mutant CH in solid tumors. Through an analysis of over 16,000 cancer patients, we demonstrate that *TET2* mutations are associated with a significant reduction in metastatic burden. Mechanistically, we show that *Tet2* deficiency prevents terminal exhaustion in $CD8^+$ tumor-infiltrating lymphocytes ($CD8^+$ TILs). This resistance is driven by DNA hypermethylation at regulatory elements of the transcription factor *Tox*, which prevents the induction of the terminal exhaustion program. Consequently, *Tet2*-deficient $CD8^+$ TILs maintain stem-like, effector-competent states that mediate durable anti-tumor immunity and suppress metastatic outgrowth. Our findings establish *TET2*-mutant CH as a natural epigenetic constraint on T-cell exhaustion and uncover a mechanistically defined pathway with translational potential for enhancing anti-tumor immune responses.

INTRODUCTION

Metastasis represents the principal cause of cancer-related mortality. Clinical metastatic disease is present in 4% to 65% of patients with solid malignancies at the time of cancer diagnosis[1]. Metastasis occurs through a complex and multi-step cascade wherein malignant cells spread beyond the primary tumor through the blood and lymph systems, colonize distant organs, and eventually manifest as metastatic lesions[2]. Immune cells recruited to metastatic sites undergo extensive reprogramming, and contribute to the formation of tumor-

68 promoting or tumor-restraining immune microenvironments[3]. Indeed, metastatic tumor-
69 infiltrating leukocytes exhibit dual effects on metastasis. Cytotoxic $CD8^+$ tumor-infiltrating
70 lymphocytes (TILs) and natural killer (NK) cells can restrain metastatic tumor cells under
71 certain conditions[4-6]. However, their anti-tumor function is frequently compromised by
72 exhaustion, characterized by upregulation of inhibitory receptors (PD-1, TIM3, LAG3) and
73 impaired effector functions within the immunosuppressive tumor microenvironment[7-9].
74 Similarly, while macrophages, neutrophils, IL-17-producing γδ T cells, and regulatory T
75 cells are commonly associated with promoting metastasis outgrowth[10-12], specific subsets
76 within these populations can exert anti-metastatic effects depending on their polarization
77 state and local microenvironmental cues. For instance, M1-polarized macrophages exhibit
78 anti-tumor activity through production of pro-inflammatory cytokines and direct
79 cytotoxicity[13,14], and presentation of tumor- antigens[15], N1-polarized neutrophils can
80 suppress tumor progression through reactive oxygen species production and immune
81 activation[16,17], and certain γδ T cell subsets demonstrate potent cytotoxic activity against
82 tumor cells and support anti-tumor immunity[18-20]. These observations indicate that the
83 phenotypic heterogeneity and functional state of tumor-infiltrating immune cells, shaped by
84 local microenvironmental cues, critically influence metastatic colonization.

85 Clonal hematopoiesis (CH), the age-associated acquisition of somatic mutations in
86 hematopoietic stem and progenitor cells, has emerged as a major source of systemic
87 inflammation and immune dysregulation. Analysis of patient samples and animal models
88 indicates that CH-derived immune cells underlie these inflammatory changes[21]. The
89 prevalence of CH in solid cancer patients is 20-30%, which is significantly higher than in

90 age-matched healthy individuals[22,23]. *DNMT3A*, *TET2*, and *ASXL1* are the most commonly
91 mutated genes driving CH in untreated solid cancer patients and in healthy individuals[23],
92 whereas exposure to cancer therapy heightens the frequency of mutations in DNA damage
93 response genes, such as *TP53*, *CHEK2,* and *PPM1D*[22]. Indeed, CH-derived mutant alleles
94 are frequently detected in tumor-infiltrating immune cells of solid cancer patients with CH[23-
95 26]. Tumor infiltration by CH-derived mutant immune cells shapes the local immune
96 microenvironment, which has been associated with tumor inflammation and poor
97 prognosis[27,28]. However, the clinical and biological implications of CH-derived immune
98 cells on solid cancer remain incompletely understood. Mouse studies revealed conflicting
99 results regarding whether CH-associated immune alterations accelerate or restrain tumor
100 growth across different cancer types[29,30]. Pan-human cancer analyses suggest CH-outcome
101 associations vary based on cancer type[22,23,31,32], and CH-driver specific outcome analyses are
102 lacking. Recently, *TET2*-mutant CH was shown to potentiate response to immune checkpoint
103 blockade in colorectal cancer (CRC), non-small cell lung cancer, melanoma, and animal
104 models[15,29,33]. Therefore, TET2 inactivation in tumor-infiltrating myeloid and lymphoid cells
105 can enhance anti-tumor immunity. Intriguingly, the potential roles of CH-derived immune
106 cells on cancer metastasis have not been clarified.

107 Here, we examined the association between CH and metastasis in a large clinical
108 cohort and further investigated how *Tet2*-deficient CH-derived immune cells regulate CRC
109 liver metastasis using conditional *Tet2* knockout mouse models.

110

111 **RESULTS**

112 ***TET2*-mutant CH is associated with lower metastatic cancer burden**

113 We analyzed CH in 16,744 non-hematological cancer patients from the MSK-IMPACT
114 cohort with matching demographic and clinical data including treatment history, cancer stage,
115 and metastatic burden[22,34]. Driver clonal hematopoiesis (CH) was defined as putative CH-
116 driver mutations with a variant allele frequency (VAF) ≥ 0.02 (Methods). Reproducing the
117 observations from the larger cohort of Bolton et al. 2020 [22], overall CH prevalence was 19.6%,
118 most commonly with *DNMT3A* (10.2%), *TET2* (3.1%), and *PPM1D* (2.6%) driver mutations
119 (Figure S1A). Prevalence increased with age, and patients with driver CH were significantly
120 older (Figures S1B and S1C). Known associations between *ASXL1* and smoking history, and
121 with *CHEK2*, *TP53*, *PPM1D* and prior exposure to cancer therapy, were recapitulated
122 (Figures S1D and S1E). Metastatic cases were more likely to have received therapy (Figure
123 S1F), and CH prevalence patterns varied by cancer type in accordance with prior studies
124 (Figures S1G and S1H).

125 To investigate a potential association between CH and cancer metastasis, we
126 compared CH prevalence in patients with and without metastatic cancer. In multivariate
127 adjusted analysis, there was a trend towards higher prevalence of driver CH in patients
128 without metastatic disease (OR 0.89, 95%CI [0.78–1.01], FDR-adjusted P = 0.109, Figure
129 1A). CH with a *TET2*-driver mutation was significantly more common in patients with local
130 compared to metastatic cancers (OR 0.64, 95%CI [0.46–0.90], P = 0.029; Figure 1A), while
131 *DNMT3A*-driven CH and other forms of CH with non-*DNMT3A*, non-*TET2* drivers were not
132 associated with metastatic status (Figure 1A). Non-driver somatic *TET2* variants were not
133 associated with metastatic status (Figure S1I). By cancer type, *TET2*-driver CH was

134 associated with lower odds of having metastatic breast cancer (multivariate logistic
135 regression, OR 0.36, $P = 0.022$), with similar trends in non–small cell lung cancer (NSCLC)
136 (OR 0.52, $P = 0.064$) and in CRC (OR 0.53, $P = 0.419$) (Figure 1B, Table S1). *TET2*-CH
137 was numerically but not statistically more common in patients with metastatic prostate cancer
138 (multivariate logistic regression, OR 1.98, $P = 0.419$). When examining metastatic status at
139 specific sites, patients with *TET2*-driver CH showed significantly reduced odds of having
140 liver (OR 0.67, $P = 0.016$) or brain metastasis (OR 0.54, $P = 0.016$), and showed a trend
141 towards lower odds of bone metastasis (OR 0.77, $P = 0.114$; Figure 1C).
142 When examining patients with metastatic disease**,** *TET2*-driver CH was linked to lower
143 metastatic disease burden as quantified by number of metastases (median and interquartile
144 range [IQR] metastasis number for *TET2*-CH, 3 [2-6], versus no CH and non-*TET2*-CH, 4
145 [2-7], $P = 0.035$; multivariate negative binomial generalized linear model IRR = 0.92, $P =$
146 0.052; Figures 1D and S1J) and involvement of fewer metastatic sites (median and IQR
147 metastasis site number for *TET2*-CH, 3 [2-5], versus no CH and non-*TET2*-CH, 3 [2-5], $P =$
148 0.006; multivariate negative binomial generalized linear model IRR = 0.92, $P = 0.035$; Figure
149 1E and S1K).
150 Overall, patients with driver CH mutations experienced modestly worse survival in
151 multivariate analysis (HR 1.06, $P = 0.0498$; Figure S1L). Strikingly, this was not driven by
152 *DNMT3A*- and *TET2*- driver CH (Figure 1F). While patients with *TET2*-driver CH trended
153 towards improved OS in multivariate analysis compared with no CH (HR 0.87, $P = 0.152$;
154 Figure 1F), patients with DDR- (HR 1.24, $P < 0.001$), cohesin- (HR 1.40, $P = 0.096$), and
155 spliceosome-driver CH (HR 1.30, $P = 0.034$) experienced worse survival (Figure 1F).

156 Therefore, solid tumor patients with *TET2*-CH are more likely to have local versus metastatic
157 cancer, those with metastatic cancer tend to have fewer metastases, and in contrast to other
158 forms of CH, *TET2*-mutant CH is not associated with worse overall survival. Based on these
159 results, we explored whether *TET2*-mutant CH could suppress cancer metastasis in animal
160 models.

161 Figure 1

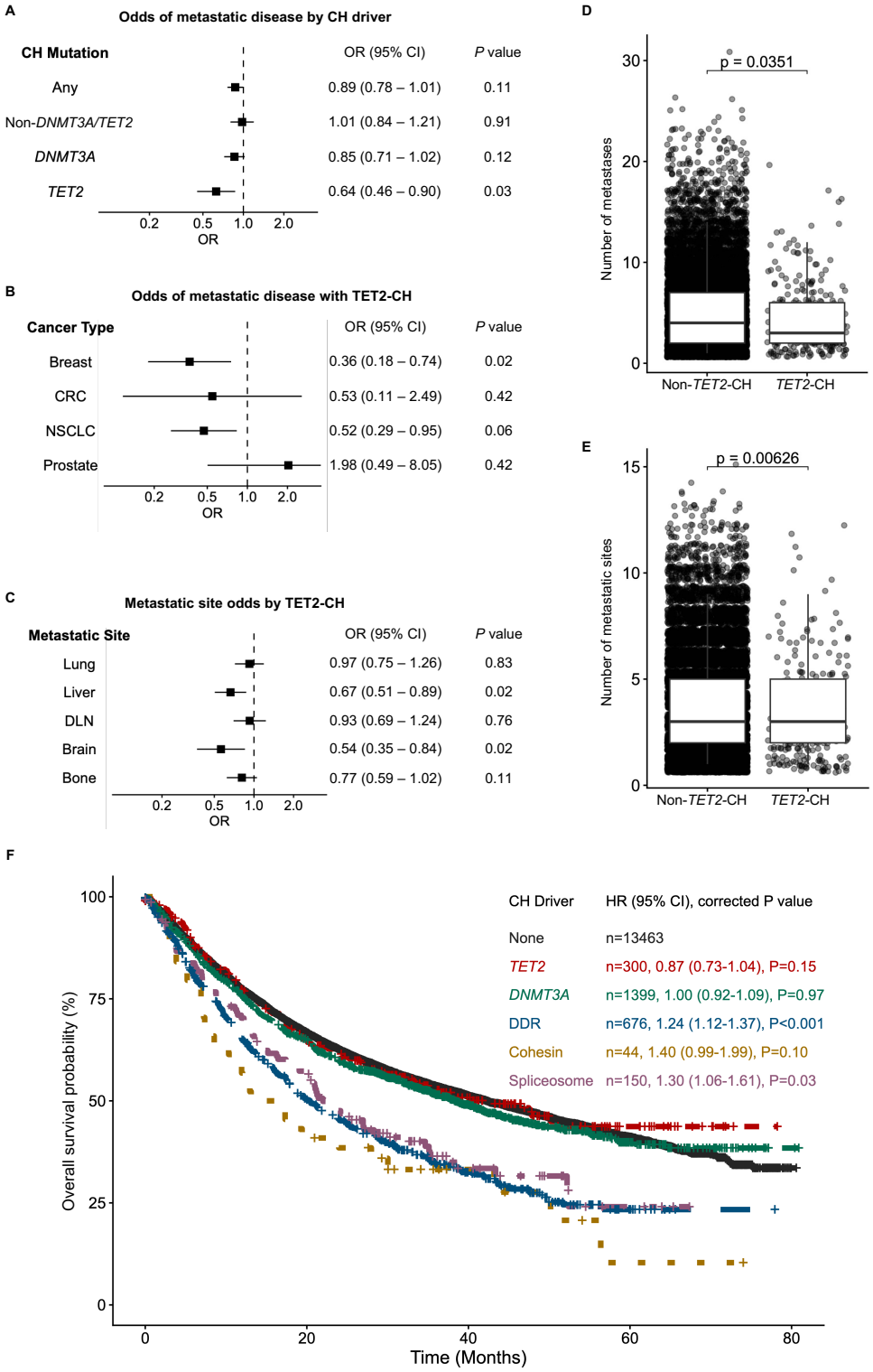
A
Odds of metastatic disease by CH driver
CH Mutation
OR (95% CI)
P value
Any
0.89 (0.78 – 1.01)
0.11
Non-DNMT3A/TET2
1.01 (0.84 – 1.21)
0.91
DNMT3A
0.85 (0.71 – 1.02)
0.12
TET2
0.64 (0.46 – 0.90)
0.03
0.2
0.5
1.0
2.0
OR
B
Odds of metastatic disease with TET2-CH
Cancer Type
OR (95% CI)
P value
Breast
0.36 (0.18 – 0.74)
0.02
CRC
0.53 (0.11 – 2.49)
0.42
NSCLC
0.52 (0.29 – 0.95)
0.06
Prostate
1.98 (0.49 – 8.05)
0.42
0.2
0.5
1.0
2.0
OR
C
Metastatic site odds by TET2-CH
Metastatic Site
OR (95% CI)
P value
Lung
0.97 (0.75 – 1.26)
0.83
Liver
0.67 (0.51 – 0.89)
0.02
DLN
0.93 (0.69 – 1.24)
0.76
Brain
0.54 (0.35 – 0.84)
0.02
Bone
0.77 (0.59 – 1.02)
0.11
0.2
0.5
1.0
2.0
OR
D
p = 0.0351
Number of metastases
30
20
10
0
Non-TET2-CH
TET2-CH
E
p = 0.00626
Number of metastatic sites
15
10
5
0
Non-TET2-CH
TET2-CH
F
Overall survival probability (%)
100
75
50
25
0
Time (Months)
0
20
40
60
80
CH Driver
HR (95% CI), corrected P value
None
n=13463
TET2
n=300, 0.87 (0.73-1.04), P=0.15
DNMT3A
n=1399, 1.00 (0.92-1.09), P=0.97
DDR
n=676, 1.24 (1.12-1.37), P<0.001
Cohesin
n=44, 1.40 (0.99-1.99), P=0.10
Spliceosome
n=150, 1.30 (1.06-1.61), P=0.03

Figure 1. *TET2*-mutant CH is associated with reduced cancer metastasis

(A) Adjusted odds of patient having metastatic versus local cancer by CH-mutant status with any CH-driver mutation, or stratified by (bottom) only *DNMT3A* driver, only *TET2* driver, and non-*TET2* non-*DNMT3A* mutant CH, with the reference of no CH. ORs and 95% confidence intervals are reported from logistic GLMs, and *P* values are FDR-adjusted.

(B) Adjusted odds of patient having metastatic versus local cancer given exposure to *TET2*-mutant CH for the four most prevalent cancer types. ORs and 95% confidence intervals are reported from logistic GLMs for each cancer type, and *P* values are FDR-adjusted (see also Table S1).

(C) Adjusted odds of metastasis occurring at specific sites given exposure to *TET2*-mutant CH. ORs and 95% confidence intervals are reported from logistic GLMs for each metastatic site, and *P* values are FDR-adjusted.

(D) The number of metastases in patients with metastatic cancer stratified by *TET2*-mutant CH presence. Differences in distributions are quantified both univariately by Wilcoxon rank sum tests, and multivariately adjusted with IRRs from negative binomial generalized linear models (Supplementary Figure1J).

(E) The distribution of the number of metastatic sites in patients with metastatic cancer stratified by *TET2*-mutant CH presence. Differences in distributions are quantified both univariately by Wilcoxon rank sum tests, and multivariately adjusted with IRRs from negative binomial generalized linear models (Supplementary Figure1K).

(F) Kaplan-Meier (KM) survival curves for overall survival of all patients, stratified by no CH mutation, and *DNMT3A*-, *TET2*-, DNA-damage-response (DDR)-, cohesin-, and spliceosome-mutant CH. Adjusted hazard ratios (HR) are reported from a Cox proportional hazards model, with the reference of no CH, and *P* values are FDR-adjusted.

CH, clonal hematopoiesis; OR, Odds ratio; GLM, generalized linear model; FDR, false discovery rate; IRR, incidence risk ratio. Detailed statistical outputs, test statistics, and model parameters for all panels in Figure 1 are provided in Table S2.

162

163 ***Tet2* deficiency in T cells inhibits CRC liver metastasis in mice**

164 We investigated the effects of hematopoietic *Tet2* deficiency on CRC metastasis to the liver,
165 since *TET2*-CH was prominently associated with reduced metastasis to this site (Figure 1C)
166 and CRC is one of the most common causes of liver metastasis. To explore the role *of Tet2*
167 loss of function in different types of immune cells on CRC metastasis, we crossed mice
168 carrying *LoxP*-flanked *Tet2* alleles ($Tet2^{fl/fl}$)[35] with $Vav1^{Cre}$ [36], $Cd4^{Cre}$ [37], $Cd19^{Cre}$ [38], and
169 $LysM^{Cre}$ [39] to generate mice with targeted *Tet2* knockout (KO) in all hematopoietic cells
170 ($Vav1^{Cre}Tet2KO$ mice), B lymphoid cells ($Cd19^{Cre}Tet2KO$ mice), T lymphoid cells
171 ($Cd4^{Cre}Tet2KO$ mice), and myeloid cells ($LysM^{Cre}Tet2KO$ mice), respectively. Venus-
172 labeled mouse intestinal tumor-derived organoid cells carrying $Apc^{\Delta 716}$, $Kras^{+/G12D}$, $Tgfbr2^{-}$
173 $^{/-}$ and $Trp^{R270H/LOH}$ mutations (Venus-$AKTP^{M/LOH}$ cells)[40], which acquired the ability to
174 metastasize to the liver, were injected into the spleen of various *Tet2* conditional KO mice
175 and $Tet2^{fl/fl}$ mice to generate CRC liver metastases (Figure 2A). After 30 days, liver metastatic
176 tumor burden (LMTB) was lower in $Vav1^{Cre}Tet2KO$ mice and $Cd4^{Cre}Tet2KO$ mice than in
177 $Tet2^{fl/fl}$ mice, while LMTB of $Cd19^{Cre}Tet2KO$ and $LysM^{Cre}Tet2KO$ mice was comparable
178 with that of $Tet2^{fl/fl}$ mice (Figures 2B and 2C; Table S3). This result suggests that *Tet2*
179 deficiency in T cells, but not in B cells or myeloid cells, is sufficient to restrict CRC liver
180 metastasis in mice.

181 Figure 2

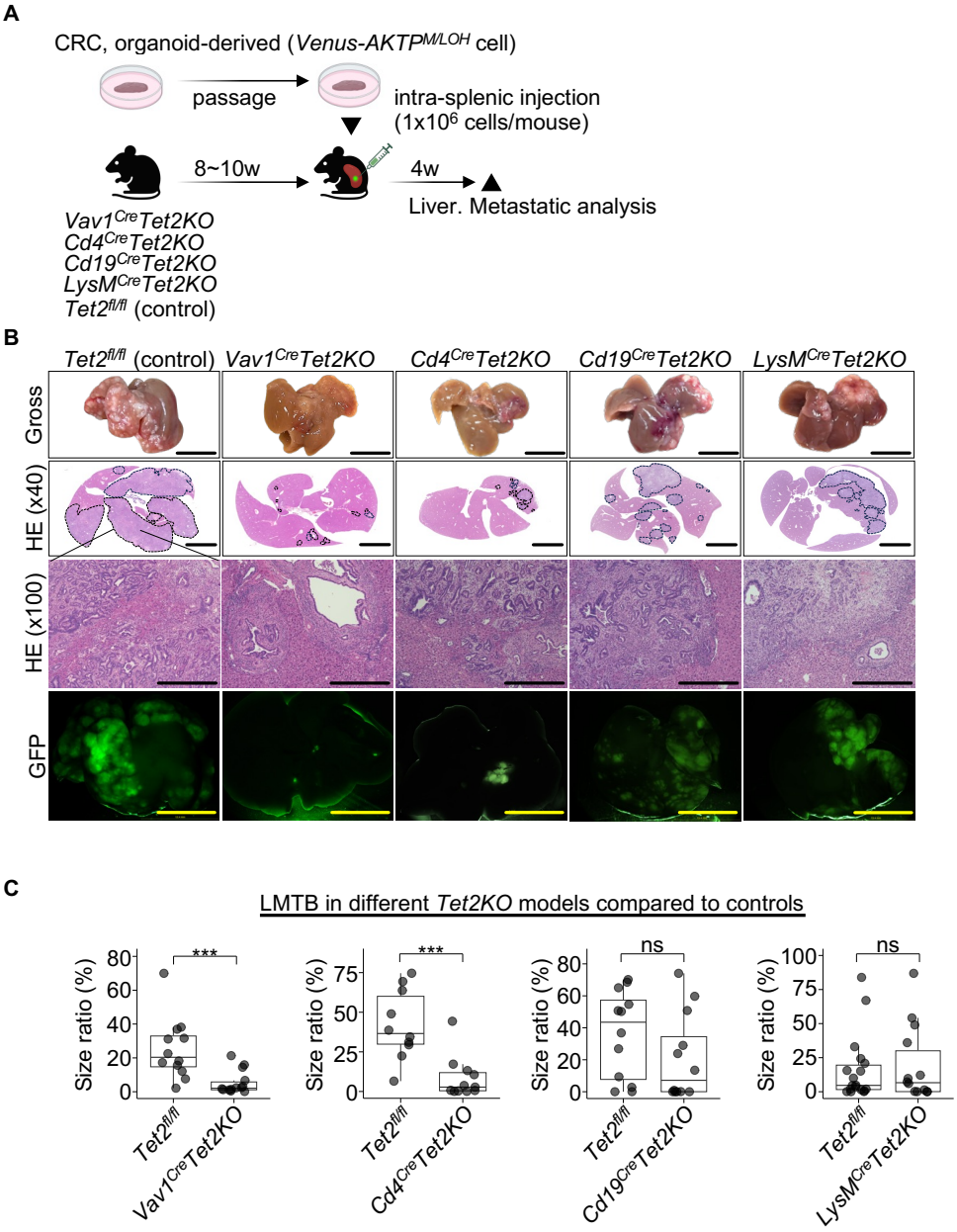
A
CRC, organoid-derived (Venus-AKTP M/LOH cell)
passage
intra-splenic injection
(1x10^6 cells/mouse)
8~10w
4w
Liver. Metastatic analysis
Vav1 Cre Tet2KO
Cd4 Cre Tet2KO
Cd19 Cre Tet2KO
LysM Cre Tet2KO
Tet2 fl/fl (control)
B
Tet2 fl/fl (control)
Vav1 Cre Tet2KO
Cd4 Cre Tet2KO
Cd19 Cre Tet2KO
LysM Cre Tet2KO
Gross
HE (x40)
HE (x100)
GFP
C
LMTB in different Tet2KO models compared to controls
Size ratio (%)
***
ns
Tet2 fl/fl
Vav1 Cre Tet2KO
Cd4 Cre Tet2KO
Cd19 Cre Tet2KO
LysM Cre Tet2KO

Figure 2. *Tet2* deficiency in T cells, but not in myeloid and B cells, inhibits the liver metastasis of CRC in mice.

(A) Schematic of the CRC liver metastasis model using cell-type-specific *Tet2* knockout mice. CRC organoid-derived Venus-*AKTP*$^{M/LOH}$ cells (1×10^6 cells/mouse) were intrasplenically injected into *Vav1*^{Cre}*Tet2KO, Cd4*^{Cre}*Tet2KO*, *Cd19*^{Cre}*Tet2KO*, *LysM*^{Cre}*Tet2KO*, and *Tet2*$^{fl/fl}$ control mice. Liver metastases were analyzed 4 weeks post-injection.

(B) Representative macroscopic (top row), HE-stained (middle rows; 40× and 100× magnification), and GFP fluorescence (bottom row) images of liver metastases. Scale bars: 1 cm (macroscopic and GFP); 5 mm (HE, 40×); 500 µm (HE, 100×).

(C) Quantification and comparisons of LMTB between different Tet2KO models and *Tet2*$^{fl/fl}$ controls. See also Table S3 for detailed quantification and statistical comparisons.

CRC, colorectal cancer; HE, hematoxylin and eosin; GFP, green fluorescent protein; LMTB, liver metastatic tumor burden. Data in (C) are pooled from 3 independent experiments (total n = 11-14 mice per group). Statistical significance was determined by Mann-Whitney U test. *$p < 0.05$, **$p < 0.01$, ***$p < 0.001$, ****$p < 0.0001$, ns = not significant.

182

183 ***Tet2* deficiency reshapes CD8$^+$ TILs through the *Tox*-exhaustion axis to enhance anti-**
184 **tumor immunity**

185 To determine which T cell subsets are regulated by *Tet2* in the anti-tumor response, we
186 compared the transcriptional profiles of CD4$^+$ TILs and CD8$^+$ TILs isolated from CRC liver
187 metastases of *Vav1^{Cre}Tet2KO* mice, *Cd4^{Cre}Tet2KO* mice, and *Tet2$^{fl/fl}$* mice (Figure 3A).
188 Principal component analysis (PCA) and heatmap clustering showed that biological
189 replicates of CD8$^+$ TILs from either *Vav1^{Cre}Tet2KO* mice or *Cd4^{Cre}Tet2KO* mice
190 (*Vav1^{Cre}/Cd4^{Cre}Tet2KO* CD8$^+$ TILs) clustered closely together but distinctly from their
191 *Tet2$^{fl/fl}$* counterparts, while *Tet2KO* CD4$^+$ TILs showed no significant separation from *Tet2$^{fl/fl}$*
192 CD4$^+$ TILs (Figures 3B and S2A, Table S4). Comparing *Vav1^{Cre}/Cd4^{Cre}Tet2KO* groups to
193 *Tet2$^{fl/fl}$* group identified substantially more differentially expressed genes (DEGs) in CD8$^+$
194 TILs than in CD4$^+$ TILs (Figure 3C). In the *Vav1^{Cre}Tet2KO* model, CD8$^+$ TILs exhibited 226
195 DEGs compared to 71 DEGs in CD4$^+$ TILs. This disparity was even more pronounced in the
196 *Cd4^{Cre}Tet2KO* model, where CD8$^+$ TILs demonstrated 209 DEGs versus only 8 DEGs in
197 CD4$^+$ TILs (FDR$<$ 0.01, |Log2 FC| > 2) (Figure 3C, Table S5-S8). These findings suggest
198 that *Tet2* deficiency affects the transcriptome of CD8$^+$ TILs more than CD4$^+$ TILs.

199 Notably, multiple exhaustion-associated genes including *Pdcd1*, *Lag3*, *Tim3*, *Tigit*,
200 *Prdm1*, *Tnfrsf9*, and *Tox* were the most significantly downregulated genes in
201 *Vav1^{Cre}/Cd4^{Cre}Tet2KO* CD8$^+$ TILs relative to *Tet2$^{fl/fl}$* CD8$^+$ TILs, suggesting attenuated
202 exhaustion programs in the absence of *Tet2*. (Figure 3D; Table S5 and S6). In CD8$^+$ TILs,
203 DEG analysis showed substantial concordance between *Vav1^{Cre}Tet2KO* and *Cd4^{Cre}Tet2KO*
204 models with 198 commonly upregulated and 89 commonly downregulated genes, including

205 downregulation of exhaustion markers *Tox* and *Pdcd1* (FDR< 0.05, |Log2 FC| > 1) (Figure
206 S2B). Using DAVID gene functional classification[41], we clustered 89 overlapping
207 downregulated genes shared by *Vav1*^{Cre}*Tet2KO* CD8^{+} TILs and *Cd4*^{Cre}*Tet2KO* CD8^{+} TILs
208 compared to *Tet2*$^{fl/fl}$ CD8^{+} TILs (Table S9A). Under stringent parameters (Table S9B), these
209 consistently downregulated genes were classified into a single cluster comprising six genes
210 associated with immunologic function, with an enrichment score of 2.59 (Figure 3E). Notably,
211 this downregulated cluster encompassed key genes linked to T-cell exhaustion, including
212 *Pdcd1*, *Lag3*, and *Tigit* (Figure 3E; Table S9C).

213 Gene Set Enrichment Analysis (GSEA)[42] was performed using the ImmuneSigDB
214 subset C7 from the Molecular Signatures Database (MSigDB)[43] to compare the genome
215 expression profiles of *Tet2KO* CD8^{+} TILs and *Tet2*$^{fl/fl}$ CD8^{+} TILs. The analysis identified 92
216 gene sets significantly enriched in *Tet2*$^{fl/fl}$ CD8^{+} TILs compared to *Cd4*^{Cre}*Tet2KO* CD8^{+} TILs,
217 five of which were specifically associated with T-cell exhaustion (Figures 3F and S3A; Table
218 S10). In the same approach, 51 gene sets related to CD8 T-cell function were enriched in
219 *Tet2*$^{fl/fl}$ CD8^{+} TILs compared to *Vav1*^{Cre}*Tet2KO* CD8^{+} TILs, including five exhaustion-
220 associated signatures (Figures 3F and S3A, Table S11). Of the 34 gene sets consistently
221 enriched in *Tet2*$^{fl/fl}$ CD8^{+} TILs relative to both *Vav1*^{Cre}*Tet2KO* and *Cd4*^{Cre}*Tet2KO*
222 counterparts, four were linked to T-cell exhaustion (Figure S3B).

223 Ingenuity Pathway Analysis (IPA) of 89 consistently downregulated genes in
224 *Vav1*^{Cre}*Tet2KO* CD8^{+} TILs and *Cd4*^{Cre}*Tet2KO* CD8^{+} TILs (Table S12) identified the
225 transcription factor *Tox* as one of the potential upstream regulators targeting genes associated
226 with T-cell exhaustion (overlap *p*-value = 0.00164) (Figure 3G; Table S12). Consistent with

227 this finding, *Tox* exhibited the greatest differential expression with the lowest *P* value among
228 all tested genes, with levels markedly higher in *Tet2*$^{fl/fl}$ CD8^{+} TILs compared to
229 *Vav1*^{Cre}/*Cd4*^{Cre}*Tet2KO* CD8^{+} TILs (*Tet2*$^{fl/fl}$ vs. *Vav1*^{Cre}*Tet2KO*, P = 0.0002; *Tet2*$^{fl/fl}$ vs.
230 *Cd4*^{Cre}*Tet2KO*, P = 0.0001; Figure S3C; Table S13).

231 Furthermore, flow cytometry analysis of CRC metastatic tumors in the liver revealed
232 a significantly higher percentage of CD8^{+} TILs co-expressing exhaustion markers Tim3 and
233 PD-1 of the *Tet2*$^{fl/fl}$ group compared with that of the *Vav1*^{Cre}/*Cd4*^{Cre}*Tet2KO* group (Figure
234 S4A; Table S14A). Indirect immunofluorescence staining further demonstrated a higher
235 number of CD8α cells co-expressing Tim3, PD-1 and Tox in tumors from the *Tet2*$^{fl/fl}$ group
236 than in the *Vav1*^{Cre}/*Cd4*^{Cre}*Tet2KO* groups (Figure S4B; Table S14B). Collectively, these
237 findings identify *Tet2* as a critical enforcer of the terminal exhaustion program, which is
238 intrinsically linked to high *Tox* expression.

239 To further validate the role of *Tet2* in regulating the antitumor functions of CD8^{+}
240 TILs, we performed CD8 T-cell depletion experiments in *Cd4*^{Cre}*Tet2KO* and *Tet2*$^{fl/fl}$ mice
241 (Figure 3H). Circulating and liver-infiltrating CD8 T cells were efficiently and specifically
242 depleted in anti-CD8α antibody-treated groups compared with PBS controls (Figures S5A
243 and S5B). CD8 T-cell depletion in *Cd4*^{Cre}*Tet2KO* mice drastically increased LMTB
244 compared to their PBS-treated controls (P = 0.007), while CD8 T-cell depletion in *Tet2*$^{fl/fl}$
245 mice had no significant effect (P = 0.396) (Figures 3I, 3J and S5C; Table S15). As a result,
246 LMTB of anti-CD8α antibody-treated *Cd4*^{Cre}*Tet2KO* mice was not significantly different
247 from that of anti-CD8α antibody-treated *Tet2*$^{fl/fl}$ mice (P = 1.0) and was comparable to that
248 of PBS-treated *Tet2*$^{fl/fl}$ mice (P = 1.0), indicating that CD8 T-cell depletion attenuated the

249 tumor-restrictive effect observed in *Tet2*-deficient mice (Figures 3I, 3J and S5C; Table S15).
250 In contrast, PBS-treated *Cd4*^{Cre}*Tet2KO* mice revealed a significantly lower LMTB compared
251 to PBS-treated *Tet2*$^{fl/fl}$ mice (P = 0.007) (Figures 3I, 3J and S5C; Table S15), consistent with
252 our earlier results. Collectively, these data demonstrate that the enhanced tumor control
253 observed in *Cd4CreTet2KO* mice requires CD8^{+} TILs.

254 Figure 3

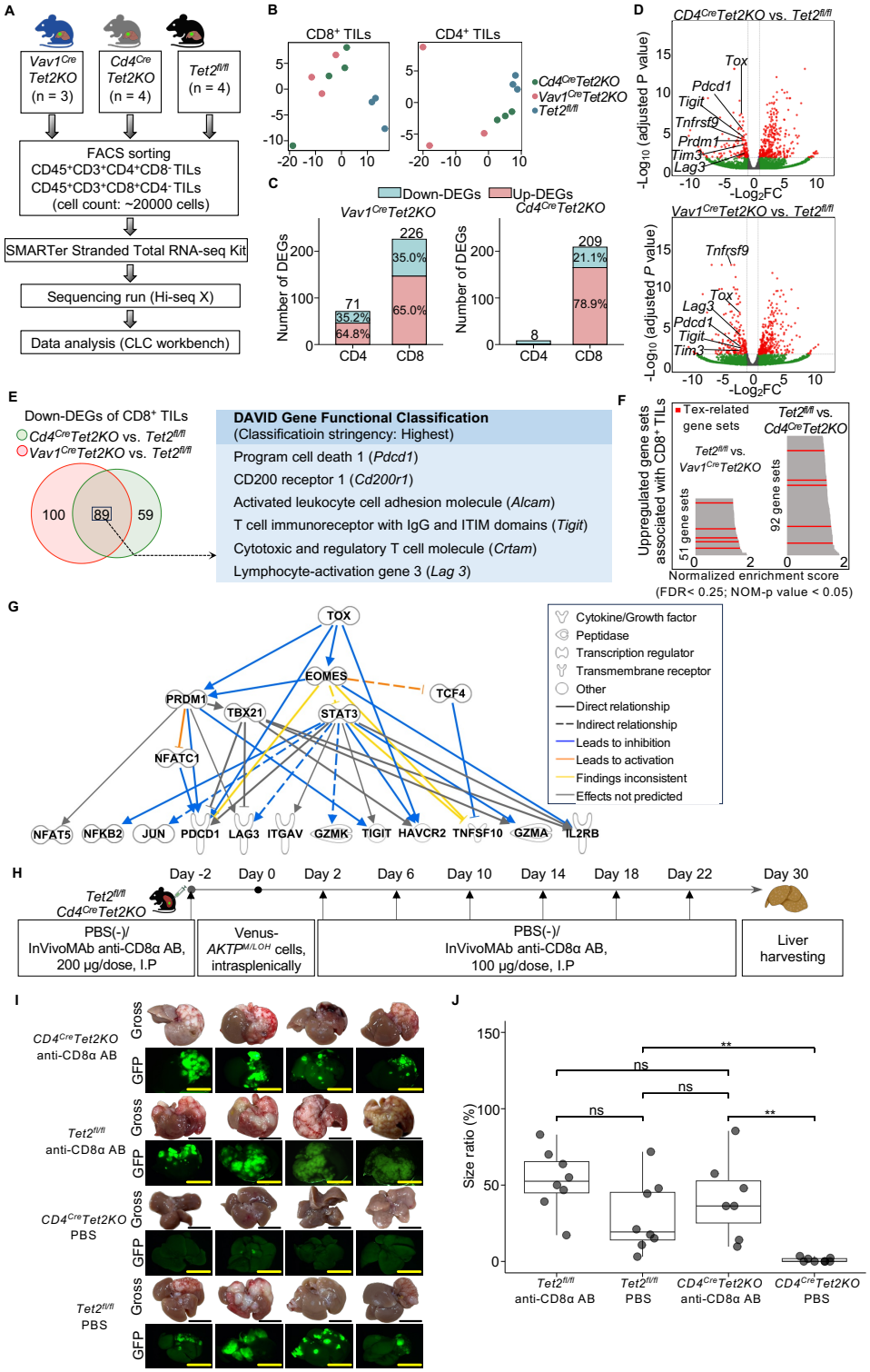
A
Vav1Cre Tet2KO (n = 3)
Cd4Cre Tet2KO (n = 4)
Tet2fl/fl (n = 4)
FACS sorting
CD45+CD3+CD4+CD8- TILs
CD45+CD3+CD8+CD4- TILs
(cell count: ~20000 cells)
SMARTer Stranded Total RNA-seq Kit
Sequencing run (Hi-seq X)
Data analysis (CLC workbench)
B
CD8+ TILs
CD4+ TILs
Cd4CreTet2KO
Vav1CreTet2KO
Tet2fl/fl
C
Down-DEGs
Up-DEGs
Vav1CreTet2KO
Cd4CreTet2KO
Number of DEGs
71
35.2%
64.8%
226
35.0%
65.0%
8
209
21.1%
78.9%
CD4
CD8
D
CD4CreTet2KO vs. Tet2fl/fl
Vav1CreTet2KO vs. Tet2fl/fl
-Log10 (adjusted P value)
-Log2FC
Tox
Pdcd1
Tigit
Tnfrsf9
Prdm1
Tim3
Lag3
E
Down-DEGs of CD8+ TILs
Cd4CreTet2KO vs. Tet2fl/fl
Vav1CreTet2KO vs. Tet2fl/fl
100
89
59
DAVID Gene Functional Classification
(Classificatioin stringency: Highest)
Program cell death 1 (Pdcd1)
CD200 receptor 1 (Cd200r1)
Activated leukocyte cell adhesion molecule (Alcam)
T cell immunoreceptor with IgG and ITIM domains (Tigit)
Cytotoxic and regulatory T cell molecule (Crtam)
Lymphocyte-activation gene 3 (Lag 3)
F
Tex-related gene sets
Tet2fl/fl vs. Cd4CreTet2KO
Tet2fl/fl vs. Vav1CreTet2KO
Upregulated gene sets associated with CD8+ TILs
51 gene sets
92 gene sets
Normalized enrichment score
(FDR< 0.25; NOM-p value < 0.05)
G
TOX
EOMES
TCF4
PRDM1
TBX21
STAT3
NFATC1
NFAT5
NFKB2
JUN
PDCD1
LAG3
ITGAV
GZMK
TIGIT
HAVCR2
TNFSF10
GZMA
IL2RB
Cytokine/Growth factor
Peptidase
Transcription regulator
Transmembrane receptor
Other
Direct relationship
Indirect relationship
Leads to inhibition
Leads to activation
Findings inconsistent
Effects not predicted
H
Tet2fl/fl
Cd4CreTet2KO
Day -2
Day 0
Day 2
Day 6
Day 10
Day 14
Day 18
Day 22
Day 30
PBS(-)/ InVivoMAb anti-CD8α AB, 200 μg/dose, I.P
Venus-AKTPM/LOH cells, intrasplenically
PBS(-)/ InVivoMAb anti-CD8α AB, 100 μg/dose, I.P
Liver harvesting
I
CD4CreTet2KO anti-CD8α AB
Tet2fl/fl anti-CD8α AB
CD4CreTet2KO PBS
Tet2fl/fl PBS
Gross
GFP
J
Size ratio (%)
ns
ns
ns
**
**
Tet2fl/fl anti-CD8α AB
Tet2fl/fl PBS
CD4CreTet2KO anti-CD8α AB
CD4CreTet2KO PBS

Figure 3. *Tet2* deficiency extensively reshapes CD8$^+$ TILs transcriptional profiles through the *Tox*-exhaustion axis to enhance anti-tumor immunity in CRC liver metastasis.

(A) Schematic of the experimental workflow for transcriptomic profiling. CD45$^+$ tumor-infiltrating leukocytes were isolated via MACS and sorted by FACS into CD4$^+$ and CD8$^+$ T cells, respectively. Total RNA was extracted from sorted populations and subjected to library preparation using SMARTer Stranded Total RNA-seq Kit, followed by high-throughput sequencing (Hi-seq X) and data analysis (CLC workbench).

(B) PCA plots of CD4 and CD8$^+$ TILs supervised by the top 200 DEGs. Gene ranking was based on combined FDR calculated by multiplying the two individual FDR from *Vav1^{Cre}Tet2KO* vs. *Tet2$^{fl/fl}$* FDR and *Cd4^{Cre}Tet2KO* vs. *Tet2$^{fl/fl}$* comparisons (selection criteria: FDR < 0.05, |Log2 FC| > 1 in both comparisons) (see also Table S4).

(C) Stacked bar plots show the number of upregulated and downregulated genes in CD4 and CD8$^+$ TILs from the comparison between *Vav1^{Cre}/Cd4^{Cre}Tet2KO* groups to *Tet2$^{fl/fl}$* group (FDR < 0.01, |Log2 FC| > 2).

(D) Volcano plots show DEGs of *Vav1^{Cre}/Cd4^{Cre}Tet2KO* CD8$^+$ TILs in comparison with *Tet2$^{fl/fl}$* CD8$^+$ TILs (FDR < 0.05, |Log2 FC| > 1).

(E) Venn diagrams display 89 overlapping down-DEGs in the comparison between *Vav1^{Cre}Tet2KO* and *Cd4^{Cre}Tet2KO* with *Tet2$^{fl/fl}$* CD8$^+$ TILs (FDR < 0.05, Log2 FC < -1). Also shown is the DAVID functional classification of these overlapping genes, highlighting a cluster associated with immunologic function (Enrichment Score: 2.59; stringent parameters).

(F) GSEA using ImmuneSigDB subset of C7 showing the enrichment of T-cell exhaustion-related signatures in *Tet2$^{fl/fl}$* CD8$^+$ TILs relative to *Vav1^{Cre}/Cd4^{Cre}Tet2KO* CD8$^+$ TILs (FDR < 0.25, nominal $p < 0.05$).

(G) Interaction network of *Tox* and T-cell exhaustion-related genes identified by IPA. The analysis was based on the 89 overlapping down-DEGs within CD8$^+$ TILs from *Vav1^{Cre}Tet2KO* and *Cd4^{Cre}Tet2KO* groups compared to the *Tet2$^{fl/fl}$* groups (FDR < 0.05, Log2 FC < -1).

(H) Schematic of the CD8 T-cell depletion experiment. Venus-*AKTP$^{M/LOH}$* cells were intrasplenically transplanted into *Cd4^{Cre}Tet2KO* or *Tet2$^{fl/f}$* mice. Anti-CD8α antibody or PBS was initiated 2 days before transplantation, and continued every 4 days throughout tumor progression.

(I) Representative macroscopic and GFP fluorescence images of liver metastases 30 days post-injection. Scale bars, 1 cm.

(J) Quantification of LMTB based on the ratio of tumor area to total liver area (%) See also Table S15 for detailed quantification and statistical comparisons.

TILs, tumor-infiltrating lymphocytes; CRC, colorectal cancer; MACS, magnetic-activated cell sorting; FACS, fluorescence-activated cell sorting; PCA, principal component analysis; DEG, differentially expressed gene; GSEA, Gene Set Enrichment Analysis; IPA, Ingenuity Pathway Analysis; GFP, green fluorescent protein; LMTB, liver metastatic tumor burden; PBS, phosphate-buffered saline. Data in (J) are compiled of 2 independent experiments (total n = 7-8 mice per group). Statistical significance in (J) was determined by pairwise Mann-Whitney U tests with Bonferroni correction for multiple comparisons. *$P < 0.05$, **$P < 0.01$, ***$P < 0.001$, ****$P < 0.0001$, ns = not significant.

255

256 ***Tet2* deficiency preserves effector function and restricts terminal differentiation of**
257 **CD8$^+$ TILs**

258 To comprehensively characterize the transcriptional landscape of *Tet2*-deficient CD8$^+$ TILs,
259 we performed single cell RNA sequencing (scRNA-seq) with V(D)J profiling. We profiled
260 16,790 and 17,367 CD45$^+$ tumor-infiltrating leukocytes isolated from liver metastatic tumors
261 of *Tet2$^{fl/fl}$* (n = 2) and *Vav1^{Cre}Tet2KO* (n = 2), respectively (Figure S6A). CD8$^+$ TIL clusters
262 were identified *in silico* from CD45$^+$ tumor-infiltrating leukocytes (Figures S6B-S6J). *In*
263 *silico*-defined CD8$^+$ TILs were subjected to unsupervised sub-clustering, resulting in the
264 identification of 9 distinct clusters, consisting of stem-like CD8 T cells (T_{SLC}, *Ly6c2^{low}*CD8
265 T_{SLC} and *Ly6c2^{high}*CD8 T_{SLC}), precursor/progenitor T cells (T_{PROG}), cytotoxic/effector-like
266 exhausted T cells (T_{EFF-1} and T_{EFF-2}), intermediate exhausted T cells (T_{INT-1} and T_{INT-2}),
267 terminally exhausted T cells (T_{TEX}), and proliferative exhausted T cells (P-T_{EX}) (Figures 4A
268 and 4B). T_{PROG} was characterized by the high expression of stem-like T-cell markers (*Sell*,
269 *Ccr7*, *Tcf7*, *Il7r* and *Id3*) along with the dual expression of effector-like and exhausted T-cell
270 markers at moderate or low levels (Figure 4C, Table S16). T_{EFF} (T4 and T5) cells displayed
271 moderate to high expression of cytolytic/effector-like and exhaustion markers. T_{TEX} (T8) cells
272 were defined by the high expression of multiple exhaustion markers and reduced expression
273 in effector-like markers (Figure 4C, Table S16). Among the spectrum of CD8$^+$ TILs, T_{PROG}
274 (T3) and T_{EFF} (T4 and T5) were predominant in *Vav1^{Cre}Tet2KO* mice, while T_{INT} (T6 and
275 T7), T_{TEX} (T8) and P-T_{EX} (T9) were dominant in control *Tet2$^{fl/fl}$* mice (Figure 4B). Among
276 stem-like CD8$^+$ TILs, *Ly6c2^{high}*T_{SLC} (T2) was markedly enriched in *Tet2$^{fl/fl}$* compared to
277 *Vav1^{Cre}Tet2KO* mice (Figure 4B). DEG analysis revealed significant upregulation of

278 exhaustion-associated genes, including *Tox, Tim3, Tnfrsf9, Eomes,* and *Gzmk*, in *Tet2*$^{fl/fl}$
279 CD8$^+$ TILs comparing to *Tet2KO* CD8$^+$ TILs, consistent with bulk RNA-seq data (Figure
280 4D; Table S17). In contrast, cytolytic and effector-related genes, such as *Klrc1, Klrk1, Ifng,*
281 *Tnf, Cd160, Ly6a, Cxcr3, Id2, Nr4a,* and *Ccl4*, were significantly upregulated in *Tet2KO*
282 CD8$^+$ TILs (Figure 4D; Table S17). Gene-set activity measured by AUCell scoring[44] further
283 demonstrated significant enrichment of effector-versus exhausted-T-cell signatures (p =
284 0.013), as well as memory- versus exhausted-T-cell signatures ($p < 0.0001$), in *Tet2KO* CD8$^+$
285 TILs compared with *Tet2*$^{fl/fl}$ CD8$^+$ TILs (Figure 4E).

286 To characterize the exhaustion phenotype, we analyzed the expression of a signature
287 comprising 42 genes consistently associated with exhausted T cells[45] (Table S18) via
288 heatmap analysis (Figure 4F). T_{SLC} (T1 and T2) clusters exhibited lower average expression
289 of most exhaustion-associated markers, consistent with their progenitor state. In contrast,
290 T_{TEX} (T8) and P-T_{EX} (T9) clusters displayed high expression across multiple exhaustion
291 markers (Figure 4F). Notably, 32 out of the 42 exhaustion-associated genes were highly
292 expressed in *Tet2*$^{fl/fl}$ CD8$^+$ TILs but downregulated in *Vav1*^{Cre}*Tet2KO* CD8$^+$ TILs (Figure
293 4F). To quantify this, we calculated the exhaustion score using this 42 gene signature. The
294 T-cell exhaustion score delineated the spectrum of exhausted T cells with positive scoring
295 values increasing toward the T_{TEX} cluster (Figure 4G). *Tet2*$^{fl/fl}$ CD8$^+$ TILs exhibited a
296 significantly higher exhaustion score than *Tet2KO* CD8$^+$ TILs (Figure 4H).

297 Using *Monocle 3*[46], we reconstructed the pseudotime trajectory of CD8$^+$ TILs to
298 investigate differentiation dynamics within the metastatic tumor microenvironment (Figure
299 4I). *Ly6c2*^{low}T_{SLC} cells were located at the root of the trajectory, consistent with their

300 progenitor-like identity. Along this trajectory, T_{PROG} cells differentiated toward T_{EFF-1} or
301 diverged toward T_{TEX} after transitioning through T_{INT} states. A subset of T_{EFF-1} cells retained
302 cytolytic capacity as inferred by effector signatures and progressed into T_{EFF-2}, while others
303 gradually lost effector function and transitioned to T_{TEX} (Figure 4I). We next examined the
304 T-cell receptor (TCR) clonotype landscape using strict clonotype calling based on the
305 combination of V(D)J genes and the nucleotide sequence of the CDR3 region[47] (Figure 4J).
306 Clonal expansion states were classified by TCR clone size: single (1 cell), small (2–5 cells),
307 medium (6–20 cells), large (21–100 cells), and hyperexpanded (>100 cells). Hyperexpanded
308 clones were predominantly enriched within T_{INT} and T_{TEX} clusters of *Tet2*$^{fl/fl}$ CD8^{+} TILs,
309 reflecting a biased differentiation toward terminal exhaustion (Figures 4J, S7A and S7B).

310 Clonal structure analysis revealed significantly greater repertoire diversity in Tet2KO
311 mice, whereas *Tet2*$^{fl/fl}$ mice exhibited marked oligoclonal dominance, particularly within
312 exhausted T cell states (Figures S7C and S7D). Clone size distribution across differentiation
313 states demonstrated that hyperexpanded clones in *Tet2*$^{fl/fl}$ were predominantly concentrated
314 in exhaustion states (T_{INT} [T6-T7], T_{TEX} [T8], and P-T_{EX} [T9]), while medium and large
315 clones were underrepresented in effector states (T_{EFF-1} and T_{EFF-2} [T4-T5]). Conversely,
316 *Tet2KO* CD8^{+} TILs displayed more balanced clone size distribution (Figures 4J and S7E-
317 S7F).

318 The TCR clonotype overlap analysis highlighted distinct differences in differentiation
319 dynamics between *Tet2*$^{fl/fl}$ and *Tet2KO* CD8^{+} TILs. In *Tet2*$^{fl/fl}$ CD8^{+} TILs, there was an
320 absence of TCR overlap between the progenitor-like states (*Ly6c2*^{high} T_{SLC} [T2] and T_{PROG}
321 [T3]) and cytolytic/effector states (T_{EFF-1} [T4] and T_{EFF-2} [T5]), indicating a restricted clonal

322 relationship (Figure 4K). Conversely, *Tet2KO* CD8^{+} TILs exhibited robust TCR overlap
323 among these populations (Figure 4K). Collectively, these data demonstrate that *Tet2*
324 deficiency prevents the oligoclonal expansion of terminally exhausted clones, while
325 preserving a broad and diverse TCR repertoire across the progenitor and effector states.

326 Figure 4

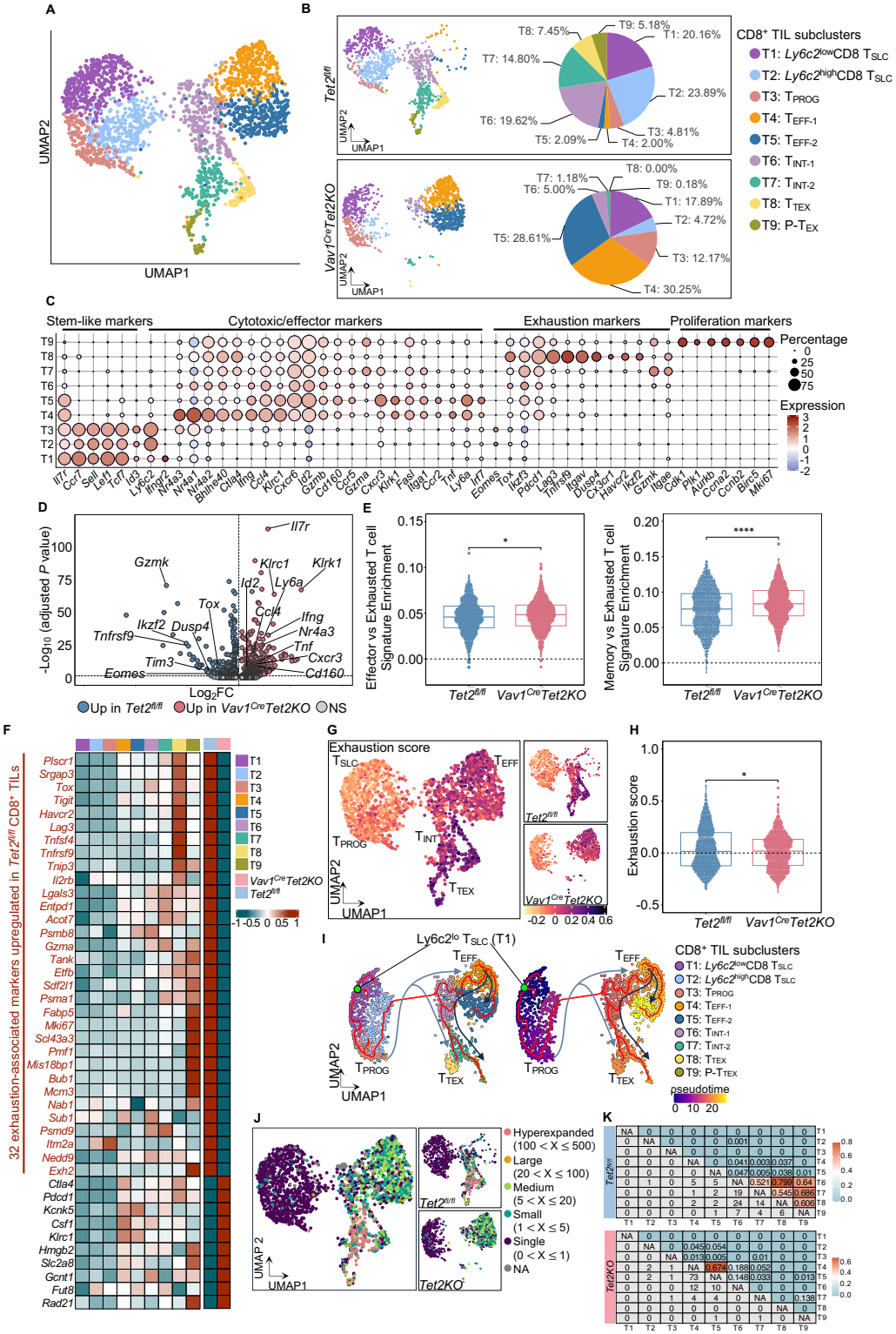
A
UMAP2
UMAP1
B
Tet2fl/fl
Vav1CreTet2KO
T8: 7.45%
T9: 5.18%
T1: 20.16%
T7: 14.80%
T2: 23.89%
T6: 19.62%
T3: 4.81%
T5: 2.09%
T4: 2.00%
T7: 1.18%
T8: 0.00%
T6: 5.00%
T9: 0.18%
T1: 17.89%
T2: 4.72%
T5: 28.61%
T3: 12.17%
T4: 30.25%
CD8+ TIL subclusters
T1: Ly6c2lowCD8 TSLC
T2: Ly6c2highCD8 TSLC
T3: TPROG
T4: TEFF-1
T5: TEFF-2
T6: TINT-1
T7: TINT-2
T8: TTEX
T9: P-TEX
C
Stem-like markers
Cytotoxic/effector markers
Exhaustion markers
Proliferation markers
Percentage
Expression
D
-Log10 (adjusted P value)
Log2FC
Up in Tet2fl/fl
Up in Vav1CreTet2KO
NS
E
Effector vs Exhausted T cell Signature Enrichment
Memory vs Exhausted T cell Signature Enrichment
F
32 exhaustion-associated markers upregulated in Tet2fl/fl CD8+ TILs
G
Exhaustion score
H
Exhaustion score
I
Ly6c2lo TSLC (T1)
pseudotime
J
Hyperexpanded (100 < X ≤ 500)
Large (20 < X ≤ 100)
Medium (5 < X ≤ 20)
Small (1 < X ≤ 5)
Single (0 < X ≤ 1)
NA
K
Tet2fl/fl
Tet2KO

Figure 4. *Tet2* deficiency preserves effector function and restricts terminal differentiation of CD8$^+$ TILs in CRC liver metastasis.

(A) Nine subclusters were labeled with different colors on the UMAP plot of the total 2,202 CD8$^+$ TILs from both *Tet2*$^{fl/fl}$ group (n = 2) and *Vav1*^{Cre}*Tet2KO* group (n = 2).

(B) UMAP plot of CD8$^+$ TIL subclusters of each mouse group (1,101 CD8$^+$ TILs for each group). The pie plots show percentages of each CD8$^+$ TIL subcluster in each group.

(C) Bubble plot showing the expression of selected marker genes among the top 50 most significant DEGs across defined clusters. The list of the top 50 most significant DEGs for each cluster are provided in Table S16.

(D) Volcano plot displaying DEGs between *Tet2*$^{fl/fl}$ and *Vav1*^{Cre}*Tet2KO* CD8$^+$ TILs, highlighting T-cell exhaustion markers and cytolytic/effector-associated genes (adjusted P value < 0.05). List of DEGs is provided in Table S17.

(E) Box plots comparing the enrichment scores of effector versus exhausted T-cell signatures (p = 0.013) and memory versus exhausted T-cell signatures (p < 0.0001) between *Tet2*$^{fl/fl}$ and *Vav1*^{Cre}*Tet2KO* CD8$^+$ TILs.

(F) Heatmap displaying the average expression of 42 exhaustion-associated marker genes across subclusters and genotypes.

(G) UMAP plot with cells labeled by exhaustion score characterize the spectrum of exhausted T cells with positive scoring values increasing toward T_{TEX}.

(H) Box plot comparing exhaustion scores between *Tet2*$^{fl/fl}$ and *Tet2KO* CD8$^+$ TILs (p = 0.046).

(I) Pseudotime trajectory of CD8$^+$ TIL subclusters inferred by Monocle3 (left), with cells ordered along the trajectory using *Ly6c2*^{low} T_{SLC} as the root (right). Arrows indicate inferred differentiation paths toward T_{EFF} and T_{TEX} states.

(J) UMAP plot with cells colored by TCR clonal size categories, showing the distribution of clones across states in each group.

(K) TCR repertoire overlap analysis using the Morisita overlap index between progenitor-like, effector, and exhausted states across groups.

TILs, tumor-infiltrating lymphocytes; CRC, colorectal cancer; UMAP, Uniform Manifold Approximation and Projection; DEG, differentially expressed gene; T_{TEX}, terminally exhausted T cell; T_{EFF}, cytotoxic/effector-like exhausted T cells; T_{SLC}, stem-like CD8 T cell; TCR, T-cell receptor.

Statistical significance in (E) and (H) was determined by Mann-Whitney U test. *$p < 0.05$, **$p < 0.01$, ***$p < 0.001$, ****$p < 0.0001$, ns = not significant.

327

328 ***Tet2* deficiency cell-intrinsically restrains terminal exhaustion and enables sustained**
329 **effector generation via progenitor preservation**

330 To directly assess whether *Tet2* regulates T-cell exhaustion in a cell-intrinsic manner, we
331 utilized an *in vitro* chronic TCR stimulation model using purified CD8 T cells from
332 *Cd4*^{Cre}*Tet2KO* and *Tet2*$^{fl/fl}$ mice. Following initial activation with plate-bound anti-CD3ε and
333 soluble anti-CD28 antibodies, cells were repeatedly re-stimulated with anti-CD3ε antibody
334 alone to mimic persistent antigen exposure (Figure 5A).

335 Flow cytometric analysis at days 7 and 12 revealed that *Tet2* deficiency selectively
336 altered exhaustion fate decisions (Figures 5B and 5C). *Tet2KO* CD8 T cells displayed
337 significantly lower frequencies of PD-1^{+}Tim3^{+}T$_{TEX}$ and PD-1^{+}Tcf1^{-}T$_{TEX}$, accompanied by a
338 significant enrichment of PD-1^{+}Tcf1^{+} PD-1^{+} progenitor exhausted T (T$_{PEX}$) cells at both
339 timepoints (Figures 5B and 5C, Table S19A and S19B). Notably, longitudinal analysis
340 further demonstrated that *Tet2* is required for progressive depletion of the progenitor
341 exhausted compartment. Between days 7 and 12, the PD-1^{+}Tcf1^{+}T$_{PEX}$ pool was markedly
342 reduced in *Tet2*$^{fl/fl}$ cultures, whereas this population was maintained in *Tet2KO* CD8 T cells,
343 despite accelerated T$_{TEX}$-cell accumulation in both genotypes (Figure 5D; Table S19C).
344 These findings validate our scRNA-seq-based observations and establish *Tet2* as a cell-
345 intrinsic regulator that promotes terminal exhaustion commitment at the expense of the
346 progenitor population under chronic TCR stimulation.

347 We next examined how *Tet2* deficiency influences memory and effector
348 differentiation states during prolonged TCR signaling. Consistent with their exhaustion
349 profile, *Tet2*$^{fl/fl}$ CD8 T cells exhibited significantly higher proportions of CD44^{+}CD62L^{-}

350 effector/effector memory ($T_{EM/EFF}$) cells, whereas *Tet2KO* CD8 T cells retained significantly
351 higher frequencies of $CD44^{+}CD62L^{+}$ central memory-like (T_{CM}) cells at both days 7 and 12
352 (Figures 5E and 5F; Table S19A and S19B). Notably, although *Tet2KO* cells displayed lower
353 $T_{EM/EFF}$ proportions at individual timepoints, longitudinal analysis revealed robust
354 differentiation capacity. From day 7 to day 12, *Tet2KO* cultures exhibited a 6.69-fold
355 expansion of the $T_{EM/EFF}$ compartment, exceeding the 3.24-fold increase observed in *Tet2*$^{fl/fl}$
356 cells (Figures 5G and 5H). Importantly, enhanced effector output in *Tet2KO* cells was
357 achieved without excessive attrition of self-renewing populations. *Tet2KO* naive CD8 T cells
358 (T_{NAIVE}) were not significantly depleted over time, and while T_{CM} frequencies declined in
359 both genotypes, *Tet2KO* cells exhibited lower fold reductions, indicating superior
360 preservation of self-renewing memory compartments (Figures 5G and 5H; Table S19C).
361 Together, these data demonstrate that *Tet2* deficiency decouples effector generation from
362 progenitor depletion, enabling sustained differentiation while preserving $Tcf1^{+}T_{PEX}$ and
363 $CD62L^{+}T_{CM}$-like reservoirs under chronic TCR stimulation.

364 Figure 5

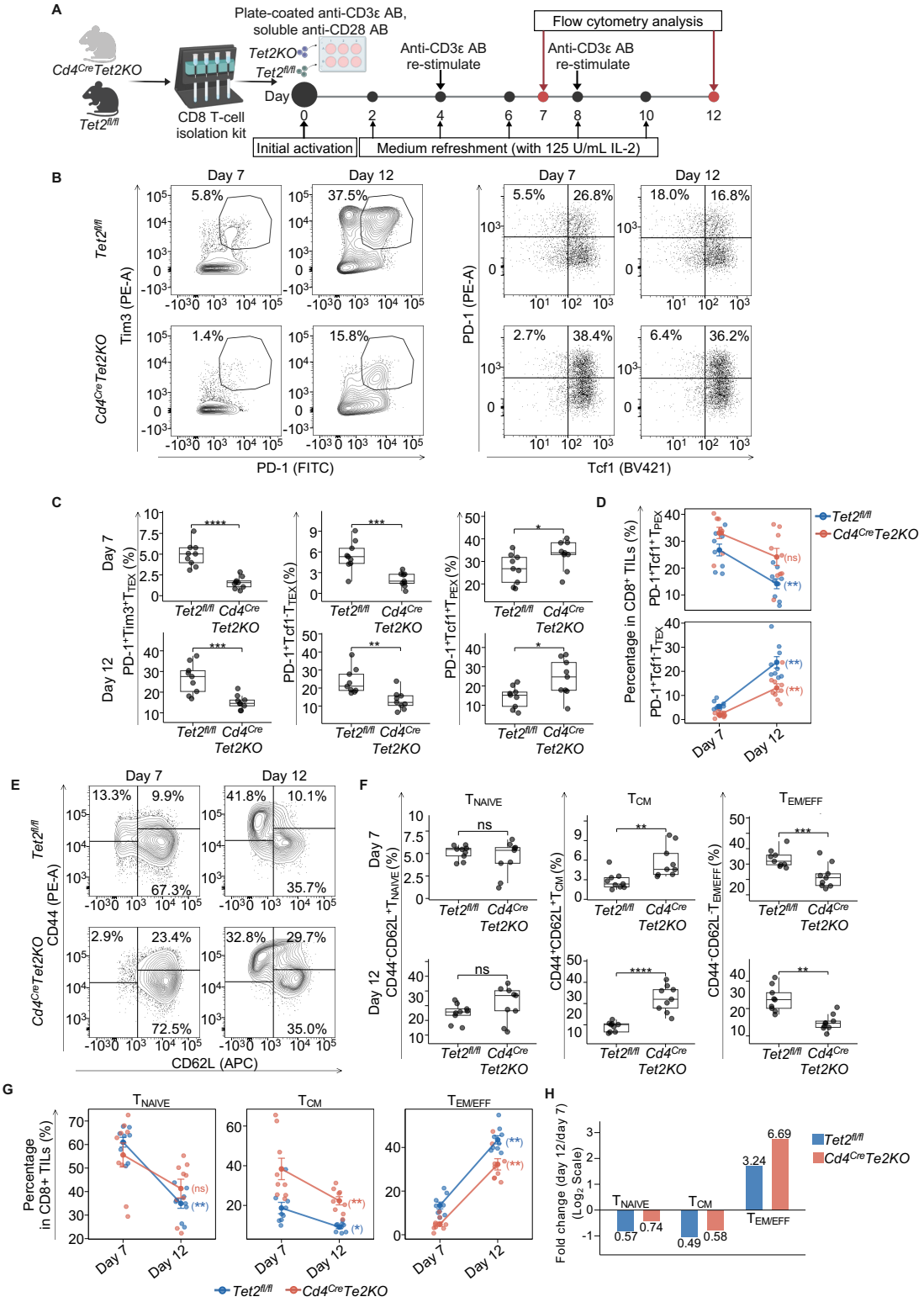
A
Plate-coated anti-CD3ε AB, soluble anti-CD28 AB
Flow cytometry analysis
Cd4CreTet2KO
Tet2fl/fl
Tet2KO
Anti-CD3ε AB re-stimulate
Anti-CD3ε AB re-stimulate
CD8 T-cell isolation kit
Day
0 2 4 6 7 8 10 12
Initial activation
Medium refreshment (with 125 U/mL IL-2)
B
Day 7
Day 12
Tim3 (PE-A)
PD-1 (FITC)
PD-1 (PE-A)
Tcf1 (BV421)
5.8%
37.5%
1.4%
15.8%
5.5%
26.8%
18.0%
16.8%
2.7%
38.4%
6.4%
36.2%
C
Day 7
Day 12
PD-1+Tim3+TTEX (%)
PD-1+Tcf1-TTEX (%)
PD-1+Tcf1+TPEX (%)
Tet2fl/fl
Cd4CreTet2KO
D
Percentage in CD8+ TILs (%)
PD-1+Tcf1+TPEX
PD-1+Tcf1-TTEX
Day 7
Day 12
E
Day 7
Day 12
CD44 (PE-A)
CD62L (APC)
13.3%
9.9%
67.3%
41.8%
10.1%
35.7%
2.9%
23.4%
72.5%
32.8%
29.7%
35.0%
F
TNAIVE
TCM
TEM/EFF
CD44+CD62L+TNAIVE (%)
CD44+CD62L+TCM (%)
CD44-CD62L-TEM/EFF (%)
ns
G
TNAIVE
TCM
TEM/EFF
Percentage in CD8+ TILs (%)
Day 7
Day 12
H
Fold change (day 12/day 7) (Log2 Scale)
TNAIVE
TCM
TEM/EFF
0.57
0.74
0.49
0.58
3.24
6.69

Figure 5. *Tet2* deficiency cell-intrinsically restrains terminal exhaustion while preserving self-renewing progenitor pools under chronic TCR stimulation.

(A) Experimental design for *in vitro* chronic TCR stimulation assay. CD8 T cells isolated from *Cd4^{Cre}Tet2KO* and *Tet2$^{fl/fl}$* mice (n = 9 per group) were activated with anti-CD3ε (2 µg/mL) and soluble anti-CD28 (2 µg/mL) antibodies, then chronically re-stimulated with anti-CD3ε antibody alone (2 µg/mL) on days 4 and 8 to model persistent antigen exposure. Cells were analyzed by flow cytometry at days 7 and 12.

(B) Representative flow cytometry plots showing expression of exhaustion markers PD-1 and Tim3 (left), and PD-1 and Tcf1 (right) at days 7 and 12 in *Tet2$^{fl/fl}$* (top row) and *Tet2KO* (bottom row) CD8 T cells.

(C) Quantification of exhaustion phenotypes. Box plots comparing frequencies of PD-1^{+}Tim3^{+}T_{TEX}, PD-1^{+}Tcf1^{-}T_{TEX}, and PD-1^{+}Tcf1^{+}T_{PEX} between *Tet2KO* and *Tet2$^{fl/fl}$* groups at day 7 (top) and day 12 (bottom). See also Table S19A and S19B for detailed quantification and statistical comparisons.

(D) Temporal dynamics of exhaustion differentiation. Longitudinal plots showing longitudinal changes from day 7 to day 12 of PD-1^{+}Tcf1^{+}T_{PEX} (top), and PD-1^{+}Tcf1^{-}T_{TEX} (bottom). See also Table S19A and S19C for detailed quantification and statistical comparisons.

(E) Representative flow cytometry plots showing CD62L and CD44 expression patterns at days 7 and 12 in *Tet2$^{fl/fl}$* (top row) and *Tet2KO* (bottom row) CD8 T cells.

(F) Quantification of memory and effector differentiation states. Box plots comparing frequencies of CD44^{-}CD62L^{+}T_{NAIVE}, CD44^{+}CD62L^{+}T_{CM}, and CD44^{+}CD62L^{-}$T_{EM/EFF}$ between *Tet2KO* and *Tet2$^{fl/fl}$* groups at day 7 and day 12. See also Table S19A and S19B for detailed quantification and statistical comparisons.

(G) Temporal dynamics of T_{NAIVE}, T_{CM}, and $T_{EM/EFF}$ populations. Longitudinal plots show longitudinal changes from day 7 to day 12 of the indicated populations (left to right). See also Table S19A and Table S19C for detailed quantification and statistical comparisons.

(H) Fold changes (day 12/day 7) on log2 scale quantifying differentiation kinetics. Numbers on bars indicate actual fold change values; y-axis is log2-transformed to show proportional changes.

TCR, T-cell receptor; T_{TEX}, terminally exhausted T cells; T_{PEX}, progenitor exhausted T cells; T_{CM}, central memory T cells; $T_{EM/EFF}$, effector memory/ effector T cells; T_{NAIVE}, Naïve T cells; AB, antibody. Data in (C), (D), (F), and (G) are compiled from three independent experiments (total n =

9 mice per group). Statistical significance for temporal comparisons (Day 7 vs. Day 12 within each genotype) determined by Wilcoxon signed-rank test (paired, two-tailed). Statistical significance for group comparisons (*Tet2*$^{fl/fl}$ vs. *Tet2KO* at each timepoint) determined by Mann-Whitney U test (unpaired, two-tailed). *$p < 0.05$, **$p < 0.01$, ***$p < 0.001$, ****$p < 0.0001$, ns = not significant.

365

366 ***Tet2* loss induces genome-wide hypermethylation and epigenetic silencing of the**
367 **exhaustion regulator *Tox* in PD-1$^+$CD8$^+$ TILs**

368 To determine whether *Tet2* loss impairs active DNA demethylation in CD8$^+$ TILs, we
369 performed whole genome bisulfite sequencing (WGBS) on activated PD-1$^+$CD8$^+$ TILs
370 isolated from liver metastatic tumors in *Vav1^{Cre}Tet2KO* and control *Tet2$^{fl/fl}$* mice (Figure 6A).
371 WGBS analysis comparing *Tet2KO* to *Tet2$^{fl/fl}$* PD-1$^+$CD8$^+$ TILs identified 19,492
372 differentially methylated regions (DMRs) across all chromosomes, of which 98.8% were
373 hypermethylated in *Tet2KO* cells (Figures S8A-C). Among these, 5,751 DMRs were mapped
374 to annotated genomic loci corresponding to 4,260 genes (Figure S8D; Table S20). A total of
375 2,644 DMRs were located in regulatory elements, including enhancer, promoter,
376 transcription start site (TSS), or CTCF-binding regions, and were designated as regulatory
377 DMRs (rDMRs) (Figure 6B; Table S21). In addition, the majority of rDMRs were distributed
378 within the enhancer or promoter regions (Figure 6B). Notably, *Tet2KO* PD-1$^+$CD8$^+$ TILs
379 exhibited a marked predominance of hypermethylated rDMRs (hyper-rDMRs; n = 2,519)
380 compared with hypomethylated rDMRs (hypo-rDMRs; n = 125) (Figure 6C). Integration of
381 WGBS with scRNA-seq revealed 22 genes with predominantly hypermethylated rDMRs that
382 were also transcriptionally downregulated in *Tet2KO* PD-1$^+$CD8$^+$ TILs compared to *Tet2$^{fl/fl}$*
383 PD-1$^+$CD8$^+$ TILs (Figures 6D; Table S22). Among these, *Tox*, a master regulator of T-cell
384 exhaustion, showed one of the most extensive methylation changes genome-wide (Figures
385 6D and S8E). A methylation impact score (total DMR count × mean absolute methylation
386 difference) (see Methods) similarly ranked *Tox* second and highlighted its widespread
387 hypermethylation across multiple regulatory regions (Figure S8F).

388 Within the *Tox* locus, differentially methylated CpG site (DMC) analysis identified
389 89 DMCs among 735 CpGs, all showing increased methylation in *Tet2KO* PD-1^{+}CD8^{+} TILs
390 relative to *Tet2*$^{fl/fl}$ PD-1^{+}CD8^{+} TILs, with a mean gain of 58.2% (Figures 6E, 6F and S8G-
391 S8I; Table S23). DMR analysis focusing on the *Tox* locus using 500bp-window screening
392 revealed 56 significant DMRs with a mean methylation increase of 47.2% (Figures 6G and
393 S8J; Table S24). Notably, *Tox* showed extensive hypermethylation at regulatory elements,
394 including 8 enhancer DMRs with mean methylation difference of 45.2%, and 4 CTCF
395 binding site DMRs with mean methylation difference of 49.3% (Figures 6G and 6H). These
396 findings indicate that *Tet2* deficiency induces broad hypermethylation at critical regulatory
397 elements of *Tox*, leading to transcriptional repression of this central exhaustion-program
398 regulator in *Tet2KO* PD-1^{+}CD8^{+} TILs.

399 Figure 6

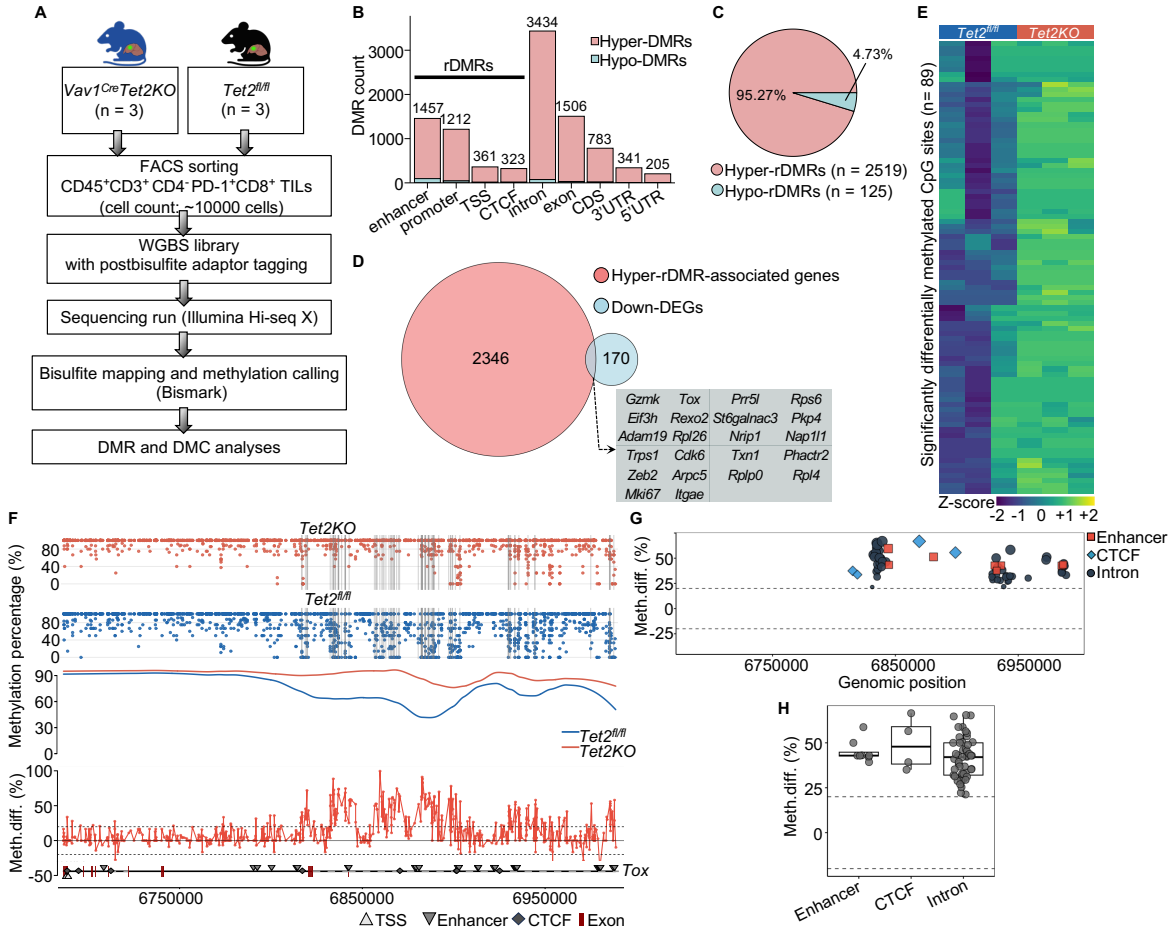
A
Vav1CreTet2KO (n = 3)
Tet2fl/fl (n = 3)
FACS sorting
CD45+CD3+ CD4- PD-1+CD8+ TILs
(cell count: ~10000 cells)
WGBS library
with postbisulfite adaptor tagging
Sequencing run (Illumina Hi-seq X)
Bisulfite mapping and methylation calling
(Bismark)
DMR and DMC analyses
B
DMR count
rDMRs
Hyper-DMRs
Hypo-DMRs
1457
1212
361
323
3434
1506
783
341
205
enhancer
promoter
TSS
CTCF
intron
exon
CDS
3'UTR
5'UTR
C
4.73%
95.27%
Hyper-rDMRs (n = 2519)
Hypo-rDMRs (n = 125)
D
Hyper-rDMR-associated genes
Down-DEGs
2346
170
Gzmk Tox Prr5l Rps6
Eif3h Rexo2 St6galnac3 Pkp4
Adam19 Rpl26 Nrip1 Nap1l1
Trps1 Cdk6 Txn1 Phactr2
Zeb2 Arpc5 Rplp0 Rpl4
Mki67 Itgae
E
Tet2fl/fl
Tet2KO
Significantly differentially methylated CpG sites (n= 89)
Z-score
-2 -1 0 +1 +2
F
Tet2KO
Tet2fl/fl
Methylation percentage (%)
Meth.diff. (%)
Tox
6750000
6850000
6950000
TSS
Enhancer
CTCF
Exon
G
Meth.diff. (%)
Enhancer
CTCF
Intron
6750000
6850000
6950000
Genomic position
H
Meth.diff. (%)
Enhancer
CTCF
Intron

Figure 6. *Tet2* loss induces genome-wide hypermethylation and epigenetic silencing of *Tox* in PD-1$^+$CD8$^+$ TILs.

(A) Schematic overview of WGBS workflow for analyzing DNA methylation in PD-1$^+$CD8$^+$ TILs.

(B) Distribution of DMRs across genomic features in *Tet2KO* vs. *Tet2$^{fl/fl}$* PD-1$^+$CD8$^+$ TILs. DMRs located at enhancer, promoter, TSS, or CTCF-binding regions, and were designated as regulatory DMRs (rDMRs).

(C) Pie chart displaying the proportion of hyper-rDMRs (n = 2519, 95.3%) versus hypo-rDMRs (n = 125, 4.7%).

(D) Venn diagram identifying 22 genes showing coordinated hypermethylation (q-value < 0.01, meth.diff > 0.2) and transcriptional downregulation (min.pct = 0.1, adjusted P value < 0.05) in *Tet2KO* PD-1$^+$CD8$^+$ TILs, including the master exhaustion regulator *Tox*.

(E) Heatmap displaying 89 significant DMCs across the *Tox* locus identified by DMC analysis, with Z-scores indicating methylation levels in *Tet2$^{fl/fl}$* and *Tet2KO* replications.

(F) Genome browser view of the *Tox* locus at CpG resolution showing methylation percentage at 735 CpG sites in *Tet2$^{fl/fl}$* (blue) and *Tet2KO* (red) PD-1$^+$CD8$^+$ TILs, with smoothed methylation trends and methylation difference plot below, the grey bars highlighting 89 significant DMCs. Gene structure indicates TSS, enhancers, CTCF binding sites, and exons.

(G) Scatter plot of methylation percentage differences across the *Tox* gene structure by DMR analysis, displaying 56 rDMRs at enhancer, CTCF, and intronic regions.

(H) Box plots of methylation percentage differences at enhancer, CTCF, and intronic regions within the *Tox* locus.

TIL, tumor-infiltrating lymphocytes; WGBS, whole genome bisulfite sequencing; DMR, differentially methylated region; DMC, differentially methylated cytosine; TSS, transcription start site; CTCF, CCCTC-binding factor; CDS, coding sequence; UTR, untranslated region; min.pct, minimum percentage of cells. For (B)-(H), statistical significance to identify DMRs and DMCs determined by *methylKit* using q-value < 0.01 and |meth.diff| ≥ 20%.

400

401 ***Tet2KO:Tet2WT* chimeric mouse model of CH demonstrates restricted tumor growth**
402 **and intrinsic resistance of *Tet2*-deficient CD8$^+$ TILs to terminal exhaustion**
403 To model the mosaicism of tumor-infiltrating immune cells observed in solid tumor patients
404 with CH, in which mutant and wild-type hematopoietic cells coexist within the tumor
405 microenvironment, we established a competitive bone marrow transplantation (BMT) mouse
406 model of CRC liver metastasis (Figure 7A). Lethally irradiated CD45.1$^+$ wild-type (WT)
407 recipients were reconstituted with mixtures of *Vav1*$^{Cre+}$*Tet2*$^{fl/fl}$ CD45.2$^+$ BM cells and *Tet2WT*
408 CD45.1$^+$/CD45.2$^+$ competitor BM cells at ratios of 1:2 or 1:3, generating *Tet2KO:Tet2WT*
409 mixed chimeras. Control *Tet2*$^{fl/fl}$*:Tet2WT* chimeras received a 1:1 mixture of *Tet2*$^{fl/fl}$ CD45.2$^+$
410 and *Tet2WT* CD45.1$^+$/CD45.2$^+$ BM cells. Four weeks post-BMT, flow cytometric analysis of
411 peripheral blood confirmed successful hematopoietic reconstitution, with donor-derived
412 CD45.2$^+$ cells constituting >95% of B220$^+$ B lymphocytes, CD11b$^+$ myeloid cells, and
413 NK1.1$^+$ natural killer cells (Figure S9A). As expected from radio-resistant host T cell
414 survival[48], approximately 25.9 ± 1.8% recipient-derived CD45.1$^+$ T cells remained within the
415 CD3$^+$ T cell population (Figure S9A). Subsequently, Venus-*AKTP*$^{M/LOH}$ CRC cells were
416 injected intrasplenically to induce liver metastases in these reconstituted chimeric mice
417 (Figure 7A).
418 Twelve weeks post-BMT, *Tet2KO* cells exhibited progressive competitive expansion
419 relative to *Tet2WT* cells across all immune cell subsets compared with the four-week post-
420 BMT baseline, with the most pronounced expansion in myeloid cell populations (Figure S9B;
421 Table S25A and S25B). In contrast, control chimeras showed no competitive advantage of
422 *Tet2*$^{fl/fl}$ cells over *Tet2WT* competitor cells, maintaining stable ratios throughout the

423 observation period (Figure S9B; Table S25A and S25B). This clonal expansion pattern
424 recapitulates the progressive outgrowth of somatic *TET2* mutant-derived CH observed in
425 human patients[49]. Within liver metastases of *Tet2KO:Tet2WT* chimeras, *Tet2KO* T cells
426 accounted for approximately 35–46% of total T cells and 23–32% of the $CD8^+$ TIL subset.
427 These frequencies were comparable to the $Tet2^{fl/fl}$ $CD45.2^+$ populations observed in controls
428 (Figure S9C; Table S25C).

429 Consistent with the restricted LMTB observed in $Vav1^{Cre}/Cd4^{Cre}Tet2KO$ mice,
430 *Tet2KO:Tet2WT* chimeric mice demonstrated significantly reduced LMTB compared to
431 $Tet2^{fl/fl}$*:Tet2WT* controls (Figures 7B and S9D). Flow cytometric analysis of liver TILs
432 revealed a markedly higher proportion of $PD\text{-}1^+Tim3^+$ T_{TEX} in both $Tet2^{fl/fl}$ $CD45.2^+$ and
433 residual recipient *Tet2WT* $CD45.1^+$ populations compared to that in *Tet2KO* $CD45.2^+$ $CD8^+$
434 TILs (Figures 7C and 7D; Table S25D). Collectively, these data demonstrate that even within
435 a competitive environment containing *Tet2WT* counterparts, *Tet2*-deficient $CD8^+$ TILs
436 exhibit an intrinsic resistance to terminal exhaustion.

437 Figure 7

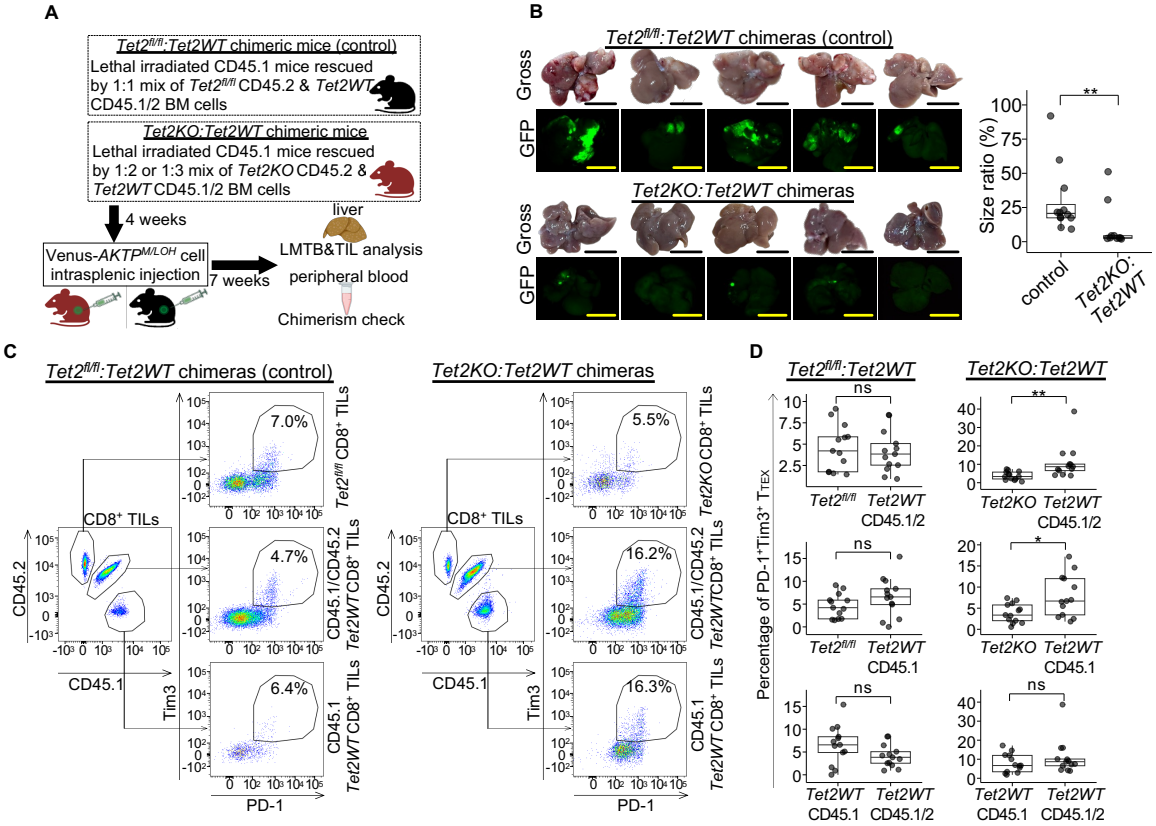
A
Tet2fl/fl:Tet2WT chimeric mice (control)
Lethal irradiated CD45.1 mice rescued by 1:1 mix of Tet2fl/fl CD45.2 & Tet2WT CD45.1/2 BM cells
Tet2KO:Tet2WT chimeric mice
Lethal irradiated CD45.1 mice rescued by 1:2 or 1:3 mix of Tet2KO CD45.2 & Tet2WT CD45.1/2 BM cells
4 weeks
Venus-AKTPM/LOH cell intrasplenic injection
7 weeks
liver
LMTB&TIL analysis
peripheral blood
Chimerism check
B
Tet2fl/fl:Tet2WT chimeras (control)
Gross
GFP
Tet2KO:Tet2WT chimeras
Size ratio (%)
control
Tet2KO: Tet2WT
C
Tet2fl/fl:Tet2WT chimeras (control)
Tet2KO:Tet2WT chimeras
CD8+ TILs
CD45.2
CD45.1
Tim3
PD-1
7.0%
4.7%
6.4%
5.5%
16.2%
16.3%
Tet2fl/fl CD8+ TILs
Tet2WT CD8+ TILs
Tet2KO CD8+ TILs
CD45.1/CD45.2
D
Tet2fl/fl:Tet2WT
Tet2KO:Tet2WT
Percentage of PD-1+Tim3+ TTEX
ns
Tet2fl/fl
Tet2WT
Tet2KO
CD45.1/2
CD45.1

Figure 7 ***Tet2KO:Tet2WT*** **chimeric mouse model of CH demonstrates restricted tumor growth and intrinsic resistance of** ***Tet2*****-deficient CD8$^+$ TILs to terminal exhaustion in CRC liver metastasis.**

(A) Experiment schema of *Tet2KO:Tet2WT* chimeric mouse model with CRC liver metastasis. Lethally irradiated CD45.1$^+$ WT-recipients were reconstituted with mixtures of *Vav1^{Cre+}Tet2$^{fl/fl}$* CD45.2$^+$ and *Tet2WT* CD45.1$^+$/CD45.2$^+$ BM cells at ratios of 1:2 or 1:3 (KO : WT competitor) to generate *Tet2KO:Tet2WT* mixed chimeras. Control *Tet2$^{fl/fl}$*:*Tet2WT* chimeras received a 1:1 mixture of *Tet2$^{fl/fl}$* CD45.2$^+$ and *Tet2WT* CD45.1$^+$/CD45.2$^+$ BM cells. Four weeks post-transplantation, Venus-*AKTP$^{M/LOH}$* colorectal cancer cells were intrasplenically injected. Chimerism was assessed in peripheral blood 8 weeks post-injection, followed by analysis of CD8$^+$ TILs and LMTB.

(B) Representative liver metastasis samples and box plot comparing LMTB between *Tet2KO:Tet2WT* chimeric mice (n = 10) and *Tet2$^{fl/fl}$*:*Tet2WT* controls (n = 12) (29.1 ± 24.1% vs. 10.6 ± 16.7%; p = 0.0076). Scale bars: 1 cm.

(C) Representative flow cytometry plots showing the proportion of PD-1$^+$Tim3$^+$ CD8 T_{TEX} in *Tet2$^{fl/fl}$* CD45.2$^+$, host-derived *Tet2WT* CD45.1$^+$, and *Tet2KO* CD45.2$^+$ CD8$^+$ TILs.

(D) Box plots comparing frequencies of PD-1$^+$Tim3$^+$ CD8 T_{TEX} across donor and host CD8$^+$ TIL populations (n = 13 per group). See also Table S25D for detailed quantification and statistical comparisons.

CH, clonal hematopoiesis; TILs, tumor-infiltrating lymphocytes; CRC, colorectal cancer; BM, bone marrow; LMTB, liver metastatic tumor burden; T_{TEX}, terminally exhausted T cells. Data in (B) and (D) are compiled of at least 2 independent experiments and presented as mean ± SD. Statistical significance was determined by Mann-Whitney U test. *p < 0.05, **p < 0.01, ***p < 0.001, ****p < 0.0001, ns = not significant.

438

439 ***Anti-PD-1 treatment suppresses CRC liver metastasis in Tet2$^{fl/fl}$ mice***

440 Given the enrichment of exhaustion markers in *Tet2$^{fl/fl}$* CD8^{+} TILs, we evaluated the
441 therapeutic efficacy of PD-1 blockade (Figure S10A). *Tet2$^{fl/fl}$* mice treated with anti-PD-1
442 antibody exhibited complete tumor eradication, whereas IgG-treated controls developed
443 profound liver metastatic growth (Figures S10B and S10C). Although IgG-treated
444 *Vav1^{Cre}Tet2KO* mice displayed reduced LMTB compared to *Tet2$^{fl/fl}$* controls (IgG-treated
445 *Vav1^{Cre}Tet2KO* vs. IgG-treated *Tet2$^{fl/fl,}$* 0.54 ± 0.39 mm2 vs. 23.53 ± 12.64 mm2, p = 0.008),
446 minimal residual tumors persisted (Figures S10B and S10C). This indicates that targeting the
447 PD-1 axis is sufficient to reverse the metastasis-permissive environment associated with
448 *Tet2*-intact hematopoiesis.

449

450 **DISCUSSION**

451 While CH is highly prevalent among patients with solid tumors, its impact on fundamental
452 aspects of cancer biology, including tumor growth, treatment response, and metastasis, has
453 remained poorly defined[21,26,50,51]. In this study, we demonstrate that *TET2*-mutant CH confers
454 protection against cancer metastasis, extending prior observations that *TET2* inactivation can
455 enhance anti-tumor immunity in settings such as chimeric antigen receptor T-cell therapy[52,53]
456 and immune checkpoint blockade[15,33]. By integrating large-scale clinical data with genetic
457 and functional mouse models, we identify *TET2*-mutant CH as a previously unrecognized
458 tumor-suppressive state that limits metastatic outgrowth.

459 In a cohort of over 16,000 solid tumor patients, we show that individuals with *TET2*-
460 driver clonal hematopoiesis have significantly lower odds of presenting with metastatic

461 disease and exhibit reduced metastatic burden. Notably, although *TET2*-mutant CH is
462 generally considered an adverse condition due to its association with increased morbidity and
463 mortality from atherosclerotic and fibrotic diseases[54-57], we did not observe a difference in
464 median survival between solid tumor patients without CH and those with *TET2*-CH. This
465 finding stands in contrast to patients harboring CH driven by mutations in DNA damage
466 response, cohesin, or spliceosome genes, who experienced significantly worse overall
467 survival, consistent with prior studies[22,23,27,58]. Together, these data suggest that the biological
468 consequences of CH are highly driver dependent, and that *TET2*-mutant CH differs
469 fundamentally from other high-risk CH genotypes in the context of solid tumor
470 microenvironments.

471 Our liver metastasis models provide functional evidence supporting a causal
472 relationship between *TET2*-mutant CH and protection from metastatic disease. Both
473 complete and chimeric pan-hematopoietic *Tet2* inactivation were sufficient to attenuate
474 metastatic outgrowth, demonstrating that this association is not merely correlative.
475 Importantly, we show that *Tet2*-deficient CD8 T cells are necessary and sufficient for the
476 anti-metastatic effect of *TET2*-mutant CH, linking this phenotype directly to adaptive
477 immune function. This finding helps reconcile prior heterogeneous reports on the impact of
478 *Tet2*-mutant CH in syngeneic tumor models, where tumor growth has been reported as
479 promoted, suppressed, or unaffected depending on tumor type, implantation site, and
480 experimental context[29,30,59]. Indeed, our patient-level analyses revealed tumor-type–specific
481 variation, with the strongest protective association observed for liver and brain metastasis.

482 Mechanistically, our data established that *Tet2* deficiency restrains metastatic
483 progression by limiting terminal CD8 T cell exhaustion. Tet2 is transcriptionally induced
484 following T cell receptor engagement[53,60] and has been shown to act as a negative regulator
485 of adaptive immunity by catalyzing DNA demethylation at key regulatory loci, thereby
486 favoring differentiation toward exhausted or regulatory states at the expense of durable
487 memory[60,61]. In the context of CH, this negative feedback is diminished. Within metastatic
488 liver lesions, *Tet2*-deficient $CD8^+$ TILs exhibit sustained methylation at regulatory elements
489 of the *Tox* locus, resulting in transcriptional repression of TOX, a master regulator of terminal
490 exhaustion[62,63]. This epigenetic constraint preserves progenitor and stem-like CD8 T cell
491 states and enables sustained effector generation under chronic antigen stimulation.

492 These findings define a TET2–DNA methylation–TOX axis as a central epigenetic
493 checkpoint governing exhaustion fate commitment in CD8 T cells. Similar mechanisms have
494 been implicated in enhanced control of chronic infection and cancer by *Tet2*-mutant CD8 T
495 cells and *Tet2*-deficient CAR-T cells[53], underscoring the generalizability of this regulatory
496 pathway. However, unrestrained T-cell activation associated with *TET2*-mutant CH may also
497 be pathological in certain contexts, including autoimmunity[64,65], immune-related toxicities
498 during immunotherapy[66], or malignant transformation following acquisition of additional
499 mutations[67,68]. Indeed, *TET2*-mutant CH is a recognized risk factor for T cell lymphoma[69] ,
500 highlighting the dual-edged nature of sustained immune activation.

501 In addition to its effects on T cells, *Tet2* loss has been shown to enhance antigen-
502 presenting capacity in macrophages[15]. While myeloid-restricted *Tet2* inactivation was
503 insufficient to suppress liver metastasis in our models, it may still contribute to improved

504 tumor control in concert with CD8 T cells. Consistent with this notion, we and others have
505 previously observed transcriptional signatures of heightened T-cell activation in colorectal
506 cancer and melanoma samples from patients with *TET2*-mutant CH[15,70]. Defining the relative
507 contributions of distinct immune lineages to other CH-associated clinical phenotypes remains
508 an important area for future investigation.

509 Several limitations of this study should be acknowledged. We were unable to directly
510 assess whether tumor-infiltrating *TET2*-mutant T lymphocytes correlate with metastatic
511 status in patients, as such data were not available. Although *TET2* is a well-established
512 negative regulator of CD8 T cell activity[53,60,71], the frequency and functional relevance of
513 *TET2*-mutant CD8 T cells within human tumors remain incompletely characterized.
514 Moreover, our experimental models focused on experimental liver metastasis and therefore
515 do not address potential effects of *TET2*-mutant CH on primary tumor growth, metastatic
516 dissemination, or circulation through blood and lymphatic compartments. While the *Cd4Cre*
517 model demonstrates that T cells are necessary and sufficient for the observed phenotype, the
518 potential contribution of other *Tet2*-deficient immune cells warrants further study. Finally,
519 the causes of death in solid tumor patients with high-risk CH are not known and may be
520 unrelated to metastatic disease.

521 In summary, we show that *TET2*-mutant CH suppresses cancer metastasis in both
522 patients and animal models by enforcing an epigenetic barrier to terminal CD8 T-cell
523 exhaustion. These findings reposition *TET2*-mutant CH as a protective modifier of tumor
524 progression and suggest that CH status may have utility as a prognostic biomarker for
525 metastatic risk, at least in certain cancers. Notably, the magnitude of metastatic suppression

526 conferred by *TET2*-mutant CH was substantial in our experimental models, approaching the
527 level of tumor control observed with immune checkpoint blockade, suggesting that
528 pharmacologic strategies designed to mimic hematopoietic *TET2* inactivation—or to target
529 downstream components of the TET2–TOX axis—could represent novel therapeutic
530 approaches for the prevention or treatment of metastatic disease.

531

532 **METHODS**

533 **Experimental model and subject details**

534 **Human study cohort**

535 Patients who were tested for clonal hematopoiesis using an MSK-IMPACT targeted
536 sequencing panel with somatic mutations from peripheral blood sequencing results curated
537 as putative drivers or non-drivers of CH in the Bolton *et al*. 2020 cohort who were also
538 evaluated for metastatic disease by Nyugen *et al*. 2022 were included in our sub-cohort
539 analysis. Study data containing anonymous patient identifiers were downloaded from
540 cBioPortal on September 4th, 2025. Using variants reported by Bolton *et al.* 2020, clonal
541 hematopoiesis (CH) was called as a putative driver mutation with variant allele fraction
542 (VAF) $\geq$ 2%. Each mutation was defined as either putative (PD) or non-putative based on its
543 role in cancer pathogenesis and recurrence in an MSKCC in-house dataset of myeloid
544 neoplasms as in Bolton *et al.* 2020. It was further was defined as either a non-myeloid PD or
545 myeloid PD based on relevance to myeloid neoplasms specifically.

546

547 **Mice**

548 *Vav1*^{Cre36}, *Cd4*^{Cre37}, *Cd19*^{Cre38}, and *LysM*^{Cre39} transgenic mice were crossed with *Tet2*$^{fl/fl}$
549 mice[35] to generate homozygous *Tet2*-knockout mice (*Vav1*^{Cre}*Tet2KO, Cd4*^{Cre}*Tet2KO*, and
550 *LysM*^{Cre}*Tet2KO*). *Tet2*$^{fl/fl}$ mice served as *Tet2* wild-type control. All mice were maintained in
551 a specific pathogen-free animal facility in the Laboratory of Animal Center, University of
552 Tsukuba. All animal procedures adhered to the The Regulations for Animal Experiments in
553 University of Tsukuba. Mouse genotyping was performed using genomic DNA extracted
554 either from tails by KAPA kit method (KAPA Biosystems) or from blood by QIAamp DNA
555 Blood Mini Kit (Qiagen). The primers used for genotyping are listed in Table S26.
556
557 **Organoid cell line**
558 Venus-labeled mouse intestinal tumor-derived organoid-originated cells simultaneously
559 carrying *Apc*$^{\Delta 716}$, *Kras*$^{+/G12D}$, *Tgfbr2*$^{-/-}$, and *Trp53*$^{R270H/LOH}$ mutations (Venus-
560 *AKTP*$^{M/LOH}$ cells) were established as previously described[40]. Venus-*AKTP*$^{M/LOH}$ cells were
561 cultured in Advanced DMEM/F-12 medium (Gibco, #2508872) supplemented with 10%
562 Fetal Bovine Serum (FBS, Hyclone, #AE25787263), 1% Penicillin-Streptomycin (PS,
563 Fujifilm, #168-23191), 0.3 μg/ml Rock inhibitor (Y27632, Fujifilm, #235-00513), 0.9 μg/ml
564 GSK-3 inhibitor (CHIR99021, R&D system, #4423), and 21 μg/ml ALK inhibitor (A8301,
565 R&D systems, #5640). For the passage, Venus-*AKTP*$^{M/LOH}$ cells were enzymatically
566 dissociated with 0.25% Trypsin at 37°C for 10 minutes and mechanically dissociated by
567 pipetting.
568
569 **Method details**

570 **Clinical cohort data processing and statistical analysis**

571 (1) Clonal hematopoiesis mutation grouping

572 Patients were categorized as having CH if they had a variant annotated as CH PD in Bolton
573 *et al.* 2020[22]. Patients were then categorized as having a *TET2* or *DNMT3A* PD only if they
574 had no other CH-defining PD variants. Using a mutually exclusive hierarchical system,
575 patients were first categorized as having a *TET2* driver, followed by a *DNMT3A*, cohesin
576 (*STAG2, RAD21, SMC1, SMC3, PDS5A, PDS5B*), spliceosome (*SF3B1, SRSF2, ZRSR2,*
577 *U2AF1*), or DNA-damage-response driver (*PPM1D, CHEK2, TP53, ATM*). For example, if
578 a patient had both a cohesin (e.g. *STAG2*) and spliceosome (*SF3B1*) PD variant, they would
579 be categorized in the cohesin group. A patient with a *TET2* and *STAG2* PD variant would
580 also be categorized in the cohesin group.

581 (2) Quantification of cancer metastatic burden

582 Patients were labelled as metastatic patient or non-metastatic patient by Nguyen *et al*.. For
583 each patient with metastatic disease, the number of metastases and metastatic sites was
584 quantified. Patients were assigned as positive or negative for cancer metastases to various
585 organs including lung, liver, draining lymph node (DLN), brain, and bone.

586 (3) Clinical cohort statistical analysis

587 The odds of metastatic disease stratified by each PD variant group was assessed using
588 multivariate logistic models to account for covariates that have previously been linked either
589 to CH prevalence or cancer outcome, including chemotherapy and radiation treatment status,
590 age, sex, smoking status, race, and cancer type. Similar models were used to assess odds of
591 metastasis within cancer types for *TET2*-driver CH. However, due to few occurrences of non-

592 metastatic cancer in *TET2*-driver CRC patients and prostate cancer patients and limitations
593 of multivariate analysis, Fisher's exact test for count data was applied in addition to the
594 logistic model to ensure robust statistical testing. (Table S1). For odds of metastasis to
595 specific sites, one model for each metastatic site allowed for patients with metastases at
596 multiple sites (such as brain and bone) to be classified as positive for all metastatic sites.

597 To assess metastatic burden, Wilcoxon rank-sum tests were used to quantify
598 differences in distribution of both number of metastases, and number of metastatic sites.
599 Further, multivariate negative binomial generalized linear models were used to account for
600 the same covariates as above.

601 Patients were categorized in a mutually exclusive manner according to the criteria
602 outlined above to investigate associations between PD variant groups and survival. Kaplan-
603 Meier survival curves and a corresponding Cox proportional hazards model were used to
604 account for covariates previously linked to survival, including age, sex, race, cancer type,
605 smoking status, chemotherapy and radiation treatment status, and metastatic status.

606 Difference in distribution of age between CH driver patients and non-CH driver
607 patients was quantified using a multivariate linear model to account for covariates associated
608 with age, including age, sex, race, cancer type, smoking status, chemotherapy and radiation
609 treatment status, and metastatic status. The association between *ASXL1* CH driver mutation
610 prevalence and smoking status was assessed using a multivariate logistic model, as were the
611 associations between DNA-damage-response CH driver mutation prevalence with treatment
612 status, and metastatic disease with treatment status. Odds of metastatic disease in patients

613 with a *TET2* CH driver mutation as opposed to a *TET2* CH non-driver mutation was also
614 assessed using a multivariate logistic model.
615 All statistical tests are two-tailed, and analyses in which multiple comparisons were
616 made were corrected for multiple hypothesis testing in a false discovery rate (FDR)
617 controlled fashion. An FDR-controlled *P* value threshold of 0.05 was used to denote
618 significance.
619
620 **Venus-AKTP$^{M/LOH}$ cell injection, liver metastasis tumor burden (LMTB) evaluation**
621 Venus-*AKTP$^{M/LOH}$* cells were used for the mouse spleen injection after at least four times of
622 passage. One million ($1x10^6$) of thoroughly dissociated Venus-*AKTP$^{M/LOH}$* cells resolved in
623 30 µl of Matrigel Matrix (Corning) were injected into mouse spleen. Mouse livers were
624 harvested 30 days post-injection and imaged as whole organs using the fluorescence stereo
625 microscope equipped with the digital color microscope camera (M165 FC/DFC450C, Leica
626 Microsystems) at 4.6x magnification to macroscopically assess the presence of Venus-
627 *AKTP$^{M/LOH}$* cell metastasis. LMTB was evaluated as previously described[72]. Briefly,
628 formalin-fixed paraffin-embedded liver sections were stained with hematoxylin and eosin
629 (H&E). The tumor burden was quantified by calculating the ratio of the total tumor area to
630 the total liver section area using a Keyence BZ-X710 microscope and BZ-X analyzer
631 software The two-tailed Mann-Whitney U test with $\alpha = 0.05$ was used to compare the size
632 ratio between the two groups.
633
634 **Antibody-based depletion of CD8 T cells**

635 Anti-CD8α antibody treatment was initiated two days prior to intrasplenic injection of Venus-
636 *AKTP*$^{M/LOH}$ cells. InVivoMAb anti-mouse CD8α antibody (clone 2.43, BioXCell, #BE0061)
637 was diluted with Phosphate-Buffered Saline (PBS) to the concentration of 1μg/μL and
638 intraperitoneally injected at an initial dose of 200 μg/mouse, followed by 6 booster injections
639 of 100 μg/mouse every 4 days throughout the tumor progression course. Control mice
640 received PBS in volumes matching those used in the anti-CD8α antibody treatment schedule.
641 Mice were sacrificed 30 days after the injection of Venus-*AKTP*$^{M/LOH}$ cells to collect the
642 whole liver for LMTB evaluation.
643
644 **Enzymatic digestion of liver metastases and isolation of tumor-infiltrating immune cells**
645 **for flow cytometry**
646 Mouse livers were harvested 30 days post-injection. Liver metastatic tumors and surrounding
647 liver tissues 0.5 cm from the edge of tumors were minced into small pieces < 1mm^3. The
648 minced tumor tissue was then digested by 15 ml of digestion buffer containing 0.75 mg/ml
649 collagenase A (Sigma-Aldrich, #10103578001) and 50 μg/ml DNase I (Worthington
650 Biochemical, #LS002139) in DMEM (Gibco, #10567-014), and incubated at 37 °C with
651 shaking at 170 rpm for 30 mins. After tissue digestion, the cell suspension was first filtered
652 through a 70-μm cell strainer (Falcon) to remove larger debris. The resulting homogenate
653 was then further filtered through a 30-μm cell strainer (Miltenyi Biotec) to obtain a single-
654 cell suspension. Any remaining undigested lumps were further dissociated by gentle pipetting.
655 DMEM supplemented with 10% FBS (Hyclone, #AE25787263) and 1% Penicillin-
656 Streptomycin (PS, Fujifilm, #168-23191) was added to terminate the digestion. The cell

657 suspension was centrifuged at 163× *g* for 7 mins at 4 °C, and then the cell pellet was
658 resuspended in 5 ml of 40% Percoll (Cytiva, #17089102) in PBS. The cell suspension was
659 then slowly and carefully dropped on top of 3 ml of Histopaque-1083 (Sigma-Aldrich,
660 #10831) without mixing and centrifuged at 1000× *g* for 20 mins in brake off mode. The cells
661 concentrated at the interface layer were carefully aspirated and added into 30 ml of FACS
662 buffer (PBS containing 2% Bovine Serum Albumin (BSA) and 2 mM EDTA) and centrifuged
663 at 800× *g* for 5 mins at 4 °C. To detect
664 exhausted T cells, the yielded cell pellet was resuspended in FACS buffer and
665 incubated with a panel of fluorophore-conjugated anti-mouse antibodies consisting of anti-
666 CD45, anti-CD3e, anti-CD4, anti-CD8α, anti-PD-1, and anti-Tim3 (Havcr2/CD366)
667 antibodies (Table S27A) before being analyzed by BD FACSAria III (BD Biosciences).
668
669 **Bulk-RNA sequencing**
670 Mouse livers were harvested 30 days post-injection. Tumor-infiltrating leukocytes yielded
671 by the same procedure as that used for flow cytometry were utilized for the CD45-positive
672 leukocyte selection. 10 μL of CD45 microbeads (Miltenyi Biotec, #130-052-301) was mixed
673 well and incubated with each $1x10^7$ cells in 90 μL of FACS buffer for 30mins at 4ºC. The
674 CD45-positive selection was then conducted using the MACS LS column and the
675 MidiMACS separator (Miltenyi Biotec), following the column-based magnetic cell-
676 separation strategy established by the manufacturer. $CD4^+$ TILs and $CD8^+$ TILs were
677 identified using a panel of fluorophore-conjugated anti-mouse antibodies consisting of CD45,
678 CD3e, CD4, and CD8α, and isolated by BD FACSAria III Cell Sorter (BD Biosciences).

679 Total RNA was isolated using RNeasy Micro Kit (Qiagen). RNA integrity number
680 (RIN) values were measured using the Agilent 2100 Bioanalyzer (Agilent Technologies).
681 Samples with RIN > 7 were subsequently used for library preparation using the SMARTer
682 Stranded Total RNA-seq Kit v2 - Pico Input Mammalian (Takara Inc.) according to the
683 manufacturer's protocol. The library size distribution and concentration were assessed with
684 the High Sensitivity DNA assay using the Agilent 2100 Bioanalyzer (Agilent Technologies).
685 Sequencing was carried out using the Illumina HiSeq X platform (Macrogen) with a standard
686 150 bp paired-end read protocol. Subsequently, the gene expression was analyzed from the
687 sequencing data using the CLC workbench version 11.0.1 (Qiagen) according the procedure
688 described previously[73]. DEGs were identified by the Differential Expression for RNA-Seq
689 tool of CLC workbench using the Wald test applying for the Against-control-group
690 comparison with the *Tet2*$^{fl/fl}$ group serving as the control. The gene expression datasets were
691 then used to identify significantly enriched gene sets for each group using GSEA[42] (GSEA
692 4.3.0, https://www.gsea-msigdb.org/gsea/index.jsp) with the ImmuneSigDB subset of C7
693 (4872 gene sets, https://www.gsea-msigdb.org/gsea/msigdb/human/collections.jsp) for
694 annotation.
695
696 **Upstream regulator analysis**
697 Overlapping downregulated DEGs within CD8^{+} TILs from *Vav1*^{Cre}*Tet2KO* and
698 *Cd4*^{Cre}*Tet2KO* groups compared to the *Tet2*$^{fl/fl}$ group (FDR< 0.05, Log2 FC < -1; Table S8)
699 were used to predict the upstream transcription factors by the Upstream Regulator Analysis
700 function of QIAGEN's IPA[74] (QIAGEN Redwood City, www.qiagen.com/ingenuity). The

701 pathway analysis was performed using the core analysis based on gene expression fold
702 change[74]. The upstream transcription regulators were called with overlap p-value < 0.01. The
703 extracted upstream regulators were then used to generate the molecular interaction network
704 by the Network and Pathway tools of IPA.
705
706 **Indirect immunofluorescence staining, co-expression cell evaluation**
707 Liver metastasis tissue collected from *Vav1*^{Cre}*Tet2KO, Cd4*^{Cre}*Tet2KO* and *Tet2*$^{fl/fl}$ groups
708 were mounted in O.C.T embeding compound (Sakura Finetek Japan Co.), frozen rapidly in
709 hexane-dry ice and stored at -80°C. The frozen tissue blocks were then sectioned at 4 µm-
710 thickness in a cryostat at -20°C. Sections were dried up in air for 60 mins at room temperature
711 (RT), fixed in 4% paraformaldehyde for 15 mins and permeabilized in 0.1% Triton X100 for
712 10 mins and incubated with protein blocking buffer (Protein block, Abcam, #ab64226).
713 Sections were then incubated with primary antibodies at 4°C for 16 hours, washed 3 times in
714 PBS for 5 mins each and subsequently incubated with secondary antibodies for 30 mins at
715 RT. Antibodies and the dilution used for immunofluorescence staining were provided in the
716 Table S27D. After three washes, tissue sections were incubated with True VIEW
717 Autofluorescence Quenching Kit (Vector Laboratories, #SP-8400-15) for 5 mins at RT and
718 mounted with 4',6-diamidino-2- 129 phenylindole (DAPI, Vectashield Mounting Medium;
719 Vector Laboratories, #H-1200).
720 The sections were imaged using the confocal laser scanning microscope (Leica TCS
721 SP8, Leica Microsystems). To quantify exhaustion phenotypes, CD8^{+} TILs co-expressing
722 PD-1, Tim3, or Tox were manually counted in 10 to 20 random intratumoral fields per sample

723 at 40× magnification. Data were expressed as the percentage of each subset relative to the
724 total $CD8^+$ TIL population. The one-way ANOVA test with $\alpha = 0.05$ was used to compare
725 the percentage of co-expressing cells between groups.
726
727 **Single-cell RNA sequencing (scRNA-seq) library preparation, data acquisition and pre-**
728 **processing**
729 Liver samples from *Vav1*^{Cre}*Tet2KO* mice and *Tet2*$^{fl/fl}$ mice were harvested at day 30 post-
730 injection, and tumor-infiltrating leukocytes were harvested using the cell processing
731 procedure that used for flow cytometry. The yielded cells were washed and resuspended in
732 PBS supplemented with 1% BSA. Cells were then incubated with Brilliant Violet 421
733 (BV421) anti-mouse CD45.2 antibody (clone 104, Biolegend, #109832) for 20 minutes at
734 4°C, followed by staining with 7-AAD viability solution (ThermoFisher Scientific, 00-6993-
735 50; 1:20) for 10 minutes on ice. CD45-positive live cells were subsequently sorted using the
736 BD FACSAria III (BD Biosciences). Isolated CD45+ live cells were processed to generate
737 barcoded 5′ gene expression (5′ GEX) libraries, together with T-cell receptor (TCR)-enriched
738 libraries, using the Chromium Next GEM Single Cell V(D)J Reagent Kits v1.1 (10x
739 Genomics, Pleasanton, CA, USA). The procedure followed the manufacturer's instructions
740 (CG000208 Rev G) and aimed to capture 10,000 cells per library. All libraries were subjected
741 to quality 150 control checks and quantified using the 2100 Bioanalyzer High Sensitivity
742 DNA Kit (Agilent 151 Technologies) and KAPA Library Quantification kit for Illumina
743 platforms (Kapa Biosystems, KK4873). The library were sequenced on the Illumina

744 NovaSeqX Plus Sequencing System (Macrogen), then mapped to the mouse genome
745 (GRCm39) and demultiplexed using CellRanger (10X Genomics, v.8.0.1).
746
747 **scRNA-seq data processing of individual samples**
748 Matrix data of each samle was processed using Seurat[75] (v.5.1.0) in RStudio (v.4.4.1).
749 Doublets were detected and removed using the "scDblFinder" function from the scDblFinder
750 package[76] (v.1.18.0) with the default estimated doublet rate. Cells with fewer than 200 or
751 more than 2,500 unique genes and those with over 5% of mitochondrial gene reads were
752 excluded. After removing ribosomal and mitochondrial genes, gene expression count data
753 was normalized using the "NormalizeData" function. Normalized data were linearly
754 transformed (scaled) with the "ScaleData" function and subjected to principal component
755 analysis (PCA) via the "RunPCA" function. Graph-based clustering was performed based on
756 gene expression profiles using the "FindNeighbors" and "FindClusters" functions. Clusters
757 were visualized using Uniform Manifold Approximation and Projection (UMAP) technique
758 via the "RunUMAP" and "DimPlot" functions.
759 Cell clusters were annotated as T lymphocytes, B lymphocytes, NK cells, and
760 myeloid cells based on marker genes identified by the "FindAllMarkers" and
761 "FindConservedMarkers" functions. For a gene to be considered a marker, a minimum of
762 25% gene-expressing cells per cluster was required, and the minimum Log2 FC in gene
763 expression of each cluster, compared to all other clusters, was set to 0.25.
764
765 **Data integration for scRNA-seq and batch correction**

766 Canonical correlation analysis (CCA) was performed to identify shared features across
767 multiple gene expression datasets using the FindIntegrationAnchors function of Seurat. Four
768 datasets (data from tumor-infiltrating leukocytes of *Tet2*$^{fl/fl}$ (n = 2) and *Vav1*^{Cre}*Tet2KO* (n =
769 2) mice) were integrated based on the identified anchors using the IntegrateData function
770 with 30 canonical correlation dimensions. The integrated data were scaled, subjected to PCA,
771 and used for graph-based clustering for cell annotation, as described above.
772
773 **scRNA-seq subclustering and cell-type annotation**
774 CD8$^+$ TIL clusters were identified and extracted from the integrated data, followed by scaling,
775 PCA-based dimensionality reduction, and unsupervised graph-based subclustering for cell
776 annotation. Subclusters that highly expressed marker genes characteristic of other immune
777 cell subsets, distinct from CD8$^+$ TILs, were excluded. Following in silico sorting, the CD8
778 T-cell dataset comprised 2,251 *Vav1*^{Cre}*Tet2KO* CD8$^+$ TILs and 1,101 *Tet2*$^{fl/fl}$ CD8$^+$ TILs. To
779 minimize discrepancies in cell numbers between the groups, downsampling was performed,
780 resulting in a balanced dataset of 1,101 CD8$^+$ TILs per group. The downsampling process
781 was repeated multiple times to ensure consistency with the original data. Cell subclusters
782 were annotated by analyzing the expression levels of canonical gene markers using Seurat's
783 "FindAllMarkers" and "FindConservedMarkers" functions.
784
785 **DEG analysis of scRNA-seq**
786 DEG analysis between *Tet2*$^{fl/fl}$ and *Vav1*^{Cre}*Tet2KO* conditions was performed using
787 "FindMarkers" function of Seurat. Genes were considered differentially expressed if they

788 met the following criteria: (i) expressed in a minimum of 10% of cells per cluster within at
789 least one condition, and (ii) exhibited a Benjamini–Hochberg adjusted p-value (adjusted p-
790 value) less than 0.05.
791
792 **Analysis of single-cell gene set activity**
793 We used the gene set comprising of 42 consistently exhausted T cell associated marker genes
794 identified by Zhang[45] to calculate the T-cell exhaustion score for single cell $CD8^+$ TIL dataset
795 using "AddModuleScore" function. The number of bins of aggregate expression levels for
796 all analyzed features was set to 24 and number of control features selected from the same bin
797 per analyzed feature was set to 100. The differential enrichment of T-cell exhaustion scores
798 between *Tet2*$^{fl/fl}$ and *Vav1*^{Cre}*Tet2KO* groups was visualized using boxplots, and statistical
799 significance was assessed via the Mann-Whitney U test.
800 We used the AUCell package[44] v.1.26.0 to analyze the Memory versus Exhausted
801 CD8 T-cell signature enrichment, and Effector versus Exhausted CD8 T-cell signature
802 enrichment for $CD8^+$ TIL dataset. The gene set
803 "*GSE9650_EXHAUSTED_VS_MEMORY_CD8_TCELL_DN"* and "*GSE9650*
804 *_EXHAUSTED_VS_MEMORY_CD8_TCELL_UP*" were obtained from the Human MSigDB
805 (v2024.1.Hs) and converted to mouse orthologs using the 'orthologs" function from the
806 babelgene package (v.22.9). Gene expression rankings were calculated for each cell using
807 the "AUCell_buildRankings" function, followed by computation of the area under the curve
808 (AUC) scores of every cells for each gene set using the "AUCell_calcAUC" function. To
809 create an aggregate Memory versus Exhausted CD8 T-cell signature, the AUC values of the

810 upregulated gene set were subtracted from those of the downregulated gene set. Similarly, to
811 calculate the aggregate Effector versus Exhausted CD8 T-cell signature enrichment, we
812 subtracted the AUC values of the downregulated gene set from those of the upregulated gene
813 set using the gene sets "GSE9650_EFFECTOR_VS_EXHAUSTED_CD8_TCELL_DN"
814 and "GSE9650_EFFECTOR_VS_EXHAUSTED_CD8_TCELL_UP" obtained from the
815 Human MSigDB (v2024.1.Hs). The differential enrichments of these gene signatures
816 between *Tet2*$^{fl/fl}$ and *Vav1*^{Cre}*Tet2KO* groups were visualized using boxplots, and statistical
817 significance was assessed via the Mann-Whitney U test.
818

819 **Single-cell trajectory inference**

820 We used *Monocle 3 toolkit*[46] (v.1.3.7) to construct the cellular pseudotime trajectories for
821 CD8 T-cell subsets. Single cell datasets were preprocessed using PCA, retaining 50
822 dimensions. Dimensionality reduction was then performed using UMAP technique. Cells
823 were clustered using the "cluster_cells" function with the Leiden algorithm, setting the
824 resolution parameter to 0.008, the number of nearest neighbors (k) to 20, and performing two
825 iterations. A principal graph representing cellular transitions was learned using the
826 "learn_graph" function with default heuristics and without partitioning the data. According
827 to previous knowledge, we selected the root cell cluster to order single cells along the
828 trajectory using the "order_cells" function. Single cell pseudotime and trajectory were
829 visualized using the "plot_cells" function.
830

831 **TCR-seq data analysis**

832 Single cell TCR-seq contig data from all samples were combined and annotated into
833 clonotypes based on shared nucleotide sequences, amino acid sequences, and V(D)J gene
834 segment usage using the "combineTCR" function of scRepertoire package[47] (v.2.3.0).
835 Clonotypes were defined using the combination of V(D)J genes (TCR/Ig) and the nucleotide
836 sequence of the CDR3 region (strict clonotype calling) throughout the analysis. The
837 clonotype data was integrated with gene expression datasets for clonal frequency calculation
838 using the "combineExpression" function. TCR clonotype similarity across cell clusters was
839 analyzed using the "clonalOverlap" function with the Morisita overlap index[47].
840 Clonal diversity was quantified using Shannon entropy and the inverse Simpson
841 index[77,78]. Clonal inequality was assessed using the Gini coefficient and Lorenz curve
842 analysis[79]. All metrics were calculated from TCR clonotype frequencies using R (v.4.4.1) in
843 RStudio.
844
845 **Whole genome bisulfite sequencing (WGBS)**
846 PD-1^{+}CD8^{+} TILs isolated from the liver metastatic tumors of *Vav1^{Cre}Tet2KO* (n = 3) and
847 *Tet2$^{fl/fl}$* (n = 3) mice were used for library preparation. Genomic DNA for WGBS was
848 extracted from sorted cells using the QIAamp DNA Blood Mini Kit (Qiagen). The library for
849 WGBS was prepared using the postbisulfite adaptor tagging (PBAT) protocol as described
850 previously[80,81]. After library preparation, library yields were quantified using the library
851 quantification kit (Takara Bio Inc.) and amplified using PrimeStar Max DNA polymerase
852 (Takara Bio Inc.). The amplified libraries were sequenced on the Illumina HiSeq X platform
853 at Macrogen.

854 WGBS data were aligned to the *Mus musculus* reference genome (GRCm39) using
855 the Bismark pipeline[82]. Differentially methylated region (DMR) analysis was performed
856 using *methylKit* package (v.1.30.0). For the genome-wide analysis, DMRs of *Tet2KO* PD-
857 1^+CD8^+ TILs in comparison to *Tet2*$^{fl/fl}$ PD-1^+CD8^+ TILs were detected by scanning non-
858 overlapping 1000bp-windows across the whole genome locus using the calculateDiffMeth
859 and getMethylDiff functions, applying a q-value < 0.01 and $|\text{meth.diff}| \geq 20\%$. For DMR
860 analysis focusing *Tox* gene, DMRs were detected by screening 500bp-windows at 250bp-
861 step, applying the same statistical thresholds as in the global analysis. Differentially
862 methylated cytosines (DMCs) within the *Tox* locus were identified at single-CpG resolution
863 with the same q-value and methylation difference cutoffs. DMRs were annotated using the
864 annotatePeakInBatch function from the ChIPpeakAnno package (v3.38), with mouse gene
865 annotations from the Gencode vM35 primary assembly and the ENCODE Registry of cCREs
866 (v3, 2021) serving as reference. DMRs overlapping enhancer, promoter, CTCF, or TSS
867 regions were classified as regulatory DMRs (rDMRs).

868 To quantify the combined regulatory impact of differential methylation on gene
869 expression, we developed a composite methylation impact score that accounts for both the
870 breadth (number of affected regulatory elements) and depth (magnitude of methylation
871 changes) of regulatory disruption. The impact score for each gene was calculated as:

872 Impact Score = (Total regulatory DMRs) × (Mean absolute methylation difference)

873 Where:

874 Total regulatory DMRs: the number of differentially methylated regions
875 (qvalue < 0.01, |methylation difference| ≥ 20%) overlapping with any regulatory
876 element (promoter, TSS, enhancer, or CTCF binding site) associated with the gene.

877 Mean absolute methylation difference: the average magnitude of methylation
878 change (%) across all regulatory DMRs for that gene.

879 This scoring approach identifies genes with extensive regulatory methylation
880 changes that are likely to have substantial effects on transcriptional control. Genes with
881 higher scores have both multiple affected regulatory elements and large-magnitude
882 methylation changes.

883

884 ***In vivo* anti-PD-1 blockade**

885 Anti-PD-1 antibody treatment was started seven days after the intrasplenic injection of
886 Venus-*AKTP*$^{M/LOH}$ cells. InVivoMAb anti-mouse PD-1 (RMP1-14, Bio X Cell, #BE0146)
887 was diluted with PBS to a final concentration of 1 μg/μL and intraperitoneally injected at a
888 dose of 10 μg/g of mouse body weight every 3 days for 6 doses in total. Control mice received
889 InVivoMAb rat IgG2a isotype control (2A3, Bio X Cell, #815022F1) following the same
890 dilution and dosage as the anti-PD-1 antibody treatment protocol. Mice were sacrificed 30
891 days after the injection of Venus-*AKTP*$^{M/LOH}$ cells to collect the whole liver for LMTB
892 evaluation.

893

894 **Competitive bone marrow transplantation (BMT) mouse model with CRC liver**
895 **metastasis**

896 Bone marrow isolation and preparation: Bone marrow cells were harvested from femurs and
897 tibias of 8-10 week-old donor mice. Bones were flushed with ice-cold PBS containing 2%
898 FBS using a 23-gauge needle. Cell suspensions were filtered through 70-μm cell strainers.
899 Viable cell counts were determined by trypan blue exclusion.

900 Lethal irradiation and competitive transplantation: Recipient CD45.1^{+} C57BL/6J
901 mice (8-12 weeks old) were lethally irradiated using an X-ray irradiator (Hitachi Power
902 Solutions MBR-1520R-3) with a split-dose protocol of 4.5 Gy twice, administered 4 hours
903 apart (total dose of 9.0 Gy) while housed in pie cages to ensure uniform radiation exposure.
904 For *Tet2KO:Tet2WT* chimeras, *Vav1Cre*$^{+}$*Tet2*$^{fl/fl}$ CD45.2^{+} bone marrow cells were mixed
905 with *Tet2WT* CD45.1^{+}/CD45.2^{+} competitor bone marrow cells at ratios of 1:2 or 1:3. Control
906 *Tet2*$^{fl/fl}$*:Tet2WT* chimeras received a 1:1 mixture of *Tet2*$^{fl/fl}$ CD45.2^{+} and *Tet2WT*
907 CD45.1^{+}/CD45.2^{+} bone marrow cells. A total of 2×10^{6} bone marrow cells in 200 μL PBS
908 were injected via retro-orbital venous plexus within 4-6 hours post-irradiation. Mice were
909 maintained in sterilized caging, food, and water were provided during the first 14 days after
910 transplantation.

911 Chimerism was assessed in peripheral blood collected via facial vein bleeding at 4
912 weeks and re-evaluated at 12 weeks post-BMT to confirm the proliferative advantage of
913 *Tet2KO* hematopoietic and lymphoid compartments. Donor cell engraftment was quantified
914 by flow cytometry analysis of CD45.1 and CD45.2 expression.

915 After confirming adequate hematopoietic reconstitution at four weeks post-BMT,
916 Venus-*AKTP*$^{M/LOH}$ cells were injected intrasplenically to establish liver metastases. Eight
917 weeks after cancer cell injection, mice were euthanized and livers were harvested and
918 processed for histological analysis. LMTB was quantified by microscopic measurement as
919 described above. Tumor-infiltrating immune cells were isolated from liver metastases by
920 enzymatic digestion as described above and subsequently analyzed by flow cytometry to
921 identify exhausted T-cell populations using a panel of fluorophore-conjugated anti-mouse
922 antibodies, consisting of anti-CD3ε, anti-CD4, anti-CD8α, anti-PD-1, anti-Tim3
923 (Havcr2/CD366), anti-CD45.1, and anti-CD45.2 antibodies (see Table S27B).
924

925 ***In vitro* modeling of CD8 T-cell exhaustion**

926 CD8 T cells were isolated from spleens of *CD4*^{Cre}*Tet2KO* mice, and *Tet2*$^{fl/fl}$ mice using the
927 Mouse CD8 T Cell Isolation Kit (Miltenyi Biotec, # 130-095-236) according to the
928 manufacturer's instructions. Purity (>90% CD45^{+}CD3^{+}CD8^{+} cells) was confirmed by flow
929 cytometry.

930 Purified CD8 T cells were seeded at 2×10^{7} cells per well in 6-well plates and activated
931 with plate-bound anti-CD3ε antibody (2 μg/mL, clone 145-2C11, BioLegend, #100340) and
932 soluble anti-CD28 antibody (2 μg/mL, clone 37.51, BioLegend, #102116) in complete RPMI
933 1640 medium supplemented with 10% FBS, 1% penicillin-streptomycin, 50 μM β-
934 mercaptoethanol, 10 mM HEPES, and recombinant mouse IL-2 (125 U/mL, PeproTech,
935 #212-12). After 4 days, T cells were harvested and transferred to fresh wells pre-coated with
936 anti-CD3 antibody alone (2 μg/mL) for chronic re-stimulation. This re-stimulation was

937 repeated on day 8. T cells were cultured for a total of 12-14 days at 37°C with 5% CO_2, with
938 medium containing IL-2 (125 U/mL) refreshed every 2-3 days.

939 At indicated timepoints (days 7 and 12), T cells were harvested and assessed for
940 exhaustion markers by flow cytometry using panels of fluorophore-conjugated anti-mouse
941 antibodies, consisting of anti-CD3ε, anti-CD8α, anti-PD-1, anti-Tim3 (Havcr2/CD366), and
942 anti-Tcf1 antibodies (see Table S27C). For intracellular staining, cells were first stained with
943 Fixable Viability Dye eFluor 780 (eBioscience, #65-0865-14), followed by cell-surface
944 markers. Cells were then fixed and permeabilized using the Foxp3/Transcription Factor
945 Staining Buffer Set (eBioscience, #00-5523-00) according to the manufacturer's instructions,
946 and stained with intracellular antibodies for 30 minutes at room temperature. Data were
947 acquired on BD FACSAria III and analyzed using FlowJo software (BD Biosciences).

948

949 **Acknowledgements**

950 We thank the staff of the associated institutions and departments for their technical assistance
951 throughout this project. We are grateful to the staff of the University of Tsukuba Animal
952 Resource Center for their support with animal care. The authors also thank Editage
953 (www.editage.com) for language editing. Figures were created using BioRender.com.

954 This work was supported by Grants-in-Aid for Scientific Research (KAKENHI:
955 JP25K19551 [M.F.], JP25K19567 [S.S.], JP25K19550 [Y.S.], JP23K15293 [K.M.], and
956 JP25H01055 [M.S.-Y.]) from the Ministry of Education, Culture, Sports, and Science of
957 Japan; AMED (JP256f0137008 [M.F.], JP23tk0124002, JP24ck0106908, JP23ck0106797,
958 JP22H04925 (PAGS), JP22zf0127009 (the Moonshot Research and Development Program)

959 and JP25gm2010006 (CREST) [M.S.-Y.]); Kobayashi Foundation for Cancer Research,
960 Japan Leukemia Research Fund, and Takeda Science [S.S.], and The Uehara Memorial
961 Foundation, Takeda Science, Kobayashi Foundation for Cancer Research, Kobayashi
962 Foundation, and the Chemo-Sero Therapeutic Research Institute [M.S.-Y.]. M.F. was
963 supported by Gilead's Research Scholars Program and a grant from The Leukemia &
964 Lymphoma Society (Grant ID: 3442-25). G.C. was supported by the National Sciences and
965 Engineering Research Council of Canada (Award 618788). R.J.V. reports funding from
966 Canadian Institutes for Health Research (PJT 203869, PJF 204160), The Princess Margaret
967 Cancer Foundation, The Leukemia and Lymphoma Society of Canada (1445410), the Brain
968 Tumour Foundation of Canada, Lymphoma Canada, Marathon of Hope Cancer Centres
969 Network Clinician Scientist Award (3256-04), Brain Canada and Cancer Research Society
970 Translational Research Grant in Brain Cancer, Cancer Research Society (1455586), and a
971 University of Toronto Hold 'Em For Life Early Career Professorship. The funders had no
972 role in the study design, data collection and analysis, or decision to publish or prepare the
973 manuscript.

974

975 **Author contributions**

976 **Conceptualization**: M.S.-Y and R.J.V.. **Data Curation**: A.N.T.L., M.F., G.C., R.J.V.,
977 T.B.N., S.S., Y.S., F.M., H.A., Y.T.M.N. **Formal analysis**: A.N.T.L., R.J.V., T.B.N., and
978 M.F. **Funding acquisition**: M.F., Y.S., K.M., R.J.V., and M.S.-Y. **Investigation**: A.N.T.L.,
979 T.B.N., Y.T.M.N., G.C. **Methodology**: A.N.T.L., T.B.N., M.F., R.J.V., F.M., H.A., H.O.,
980 M.N., M.K., M.O., and M.S.-Y. **Project administration**: A.N.T.L., M.F., R.J.V., and M.S.-

Y. **Resources**: A.N.T.L., M.F., T.B.N., G.C., Y.T.M.N., F.M., H.A., S.S., K.M., T.S., H.O., M.N., M.O., S.I., S.S., Y.S., M.K., R.J.V., and M.S.-Y. **Software**: A.N.T.L., R.J.V., M.F., and T.B.N. **Supervision**: M.F., R.J.V., and M.S.-Y. **Validation**: A.N.T.L., R.J.V., and T.B.N. **Visualization**: A.N.T.L., R.J.V., and M.F. **Writing-Original Draft**: A.N.T.L., R.J.V., M.F., and M.S.-Y. **Writing-Review & Editing**: A.N.T.L., M.F., R.J.V., G.C., and M.S.-Y.

Declaration of Interests

M.F. received research support from Gilead Sciences (Research Scholars Program) and The Leukemia & Lymphoma Society. M.S.-Y. received research support from the Takeda Science Foundation and the Chemo-Sero Therapeutic Research Institute. R.J.V. is co-inventor on a patent, “Clonal Hematopoiesis as a Biomarker”. The authors declare no other competing interests.

Declaration of generative AI and AI-assisted technologies

During manuscript preparation, generative AI tools were used solely for language editing and clarity improvement. The authors reviewed and validated all content and take full responsibility for the manuscript.

RESOURCE AVAILABILITY

Lead contact

1000 Further information and requests for resources and reagents should be directed to and will be
1001 fulfilled by the lead contact, Mamiko Sakata-Yanagimoto (sakatama@md.tsukuba.ac.jp).

1002 **Materials availability**

1003 This study did not generate new unique reagents.

1004 **Data and code availability**

1005 Statistical source data and detailed results for human cohort analyses (Figure 1 and Figure
1006 S1) are provided in Table S1 and Table S2. All original code will be deposited at GitHub and
1007 made publicly available as of the date of publication. The code for scRNA-seq and WGBS
1008 analysis will be available at: [Link will be provided upon publication]. The code for clonal
1009 hematopoiesis correlation analysis is available at:
1010 https://github.com/GiacomoCampo/msk_ch_correlations. Any additional information
1011 required to reanalyze the data reported in this paper is available from the lead contact upon
1012 request.

1013 **REFERENCES**

1014 1. Luyendijk, M., Visser, O., Blommestein, H.M., de Hingh, I., Hoebers, F.J.P., Jager, A., Sonke,
1015 G.S., de Vries, E.G.E., Uyl-de Groot, C.A., and Siesling, S. (2023). Changes in survival in de
1016 novo metastatic cancer in an era of new medicines. J Natl Cancer Inst *115*, 628-635.
1017 10.1093/jnci/djad020.

1018 2. Kitamura, T., Qian, B.Z., and Pollard, J.W. (2015). Immune cell promotion of metastasis.
1019 Nat Rev Immunol *15*, 73-86. 10.1038/nri3789.

1020 3. Edwards, S.C., Hoevenaar, W.H.M., and Coffelt, S.B. (2021). Emerging immunotherapies
1021 for metastasis. British Journal of Cancer *124*, 37-48. 10.1038/s41416-020-01160-5.

1022 4. Arias-Badia, M., Chang, R., and Fong, L. (2024). γδ T cells as critical anti-tumor immune
1023 effectors. Nature Cancer *5*, 1145-1157. 10.1038/s43018-024-00798-x.

1024 5. Dean, I., Lee, C.Y.C., Tuong, Z.K., Li, Z., Tibbitt, C.A., Willis, C., Gaspal, F., Kennedy, B.C.,
1025 Matei-Rascu, V., Fiancette, R., et al. (2024). Rapid functional impairment of natural killer
1026 cells following tumor entry limits anti-tumor immunity. Nature Communications *15*, 683.
1027 10.1038/s41467-024-44789-z.

1028 6. Portale, F., and Di Mitri, D. (2023). NK Cells in Cancer: Mechanisms of Dysfunction and
1029 Therapeutic Potential. Int J Mol Sci *24*. 10.3390/ijms24119521.

1030 7. Xie, F., Zhou, X., Su, P., Li, H., Tu, Y., Du, J., Pan, C., Wei, X., Zheng, M., Jin, K., et al. (2022).
1031 Breast cancer cell-derived extracellular vesicles promote CD8+ T cell exhaustion via TGF-β
1032 type II receptor signaling. Nature Communications *13*, 4461. 10.1038/s41467-022-31250-
1033 2.

1034 8. Baessler, A., and Vignali, D.A.A. (2024). T Cell Exhaustion. Annu Rev Immunol *42*, 179-206.
1035 10.1146/annurev-immunol-090222-110914.

1036 9. Gavil, N.V., Scott, M.C., Weyu, E., Smith, O.C., O'Flanagan, S.D., Wijeyesinghe, S., Lotfi-
1037 Emran, S., Shiao, S.L., Vezys, V., and Masopust, D. (2023). Chronic antigen in solid tumors
1038 drives a distinct program of T cell residence. Sci Immunol *8*, eadd5976.
1039 10.1126/sciimmunol.add5976.

1040 10. Coffelt, S.B., Kersten, K., Doornebal, C.W., Weiden, J., Vrijland, K., Hau, C.-S., Verstegen,
1041 N.J.M., Ciampricotti, M., Hawinkels, L.J.A.C., Jonkers, J., and de Visser, K.E. (2015). IL-17-
1042 producing γδ T cells and neutrophils conspire to promote breast cancer metastasis. Nature
1043 *522*, 345-348. 10.1038/nature14282.

1044 11. Wu, P., Wu, D., Ni, C., Ye, J., Chen, W., Hu, G., Wang, Z., Wang, C., Zhang, Z., Xia, W., et al.
1045 (2014). γδT17 cells promote the accumulation and expansion of myeloid-derived
1046 suppressor cells in human colorectal cancer. Immunity *40*, 785-800.
1047 10.1016/j.immuni.2014.03.013.

1048 12. Hedrick, C.C., and Malanchi, I. (2022). Neutrophils in cancer: heterogeneous and
1049 multifaceted. Nature Reviews Immunology *22*, 173-187. 10.1038/s41577-021-00571-6.

1050 13. de Visser, K.E., and Joyce, J.A. (2023). The evolving tumor microenvironment: From cancer
1051 initiation to metastatic outgrowth. Cancer Cell *41*, 374-403. 10.1016/j.ccell.2023.02.016.

1052 14. Xu, J., Ding, L., Mei, J., Hu, Y., Kong, X., Dai, S., Bu, T., Xiao, Q., and Ding, K. (2025). Dual
1053 roles and therapeutic targeting of tumor-associated macrophages in tumor
1054 microenvironments. Signal Transduction and Targeted Therapy *10*, 268. 10.1038/s41392-
1055 025-02325-5.

1056 15. Herbrich, S., Chaib, M., Anandhan, S., Andrewes, S.W., Nagarajan, A., Guan, B., Gandhi, N.,
1057 Gilliam, J., Radovich, M., and Sharma, P. (2026). *TET2* mutant clonal hematopoiesis
1058 enhances macrophage antigen presentation and improves immune checkpoint therapy in
1059 solid tumors. Cancer Cell *44*, 187-202.e187. 10.1016/j.ccell.2025.09.011.

1060 16. Carnevale, S., Di Ceglie, I., Grieco, G., Rigatelli, A., Bonavita, E., and Jaillon, S. (2023).
1061 Neutrophil diversity in inflammation and cancer. Front Immunol *14*, 1180810.
1062 10.3389/fimmu.2023.1180810.

1063 17. Jaillon, S., Ponzetta, A., Di Mitri, D., Santoni, A., Bonecchi, R., and Mantovani, A. (2020).
1064 Neutrophil diversity and plasticity in tumour progression and therapy. Nat Rev Cancer *20*,
1065 485-503. 10.1038/s41568-020-0281-y.

1066 18. Sebestyen, Z., Prinz, I., Déchanet-Merville, J., Silva-Santos, B., and Kuball, J. (2020).
1067 Translating gammadelta (γδ) T cells and their receptors into cancer cell therapies. Nature
1068 Reviews Drug Discovery *19*, 169-184. 10.1038/s41573-019-0038-z.

1069 19. Bruni, E., Cimino, M.M., Donadon, M., Carriero, R., Terzoli, S., Piazza, R., Ravens, S., Prinz,
1070 I., Cazzetta, V., Marzano, P., et al. (2022). Intrahepatic CD69(+)Vδ1 T cells re-circulate in
1071 the blood of patients with metastatic colorectal cancer and limit tumor progression. J
1072 Immunother Cancer *10*. 10.1136/jitc-2022-004579.

1073 20. Wu, Y., Kyle-Cezar, F., Woolf, R.T., Naceur-Lombardelli, C., Owen, J., Biswas, D., Lorenc, A.,
1074 Vantourout, P., Gazinska, P., Grigoriadis, A., et al. (2019). An innate-like Vδ1(+) γδ T cell
1075 compartment in the human breast is associated with remission in triple-negative breast
1076 cancer. Sci Transl Med *11*. 10.1126/scitranslmed.aax9364.

1077 21. Jaiswal, S., and Ebert, B.L. (2019). Clonal hematopoiesis in human aging and disease.
1078 Science *366*, eaan4673. doi:10.1126/science.aan4673.

1079 22. Bolton, K.L., Ptashkin, R.N., Gao, T., Braunstein, L., Devlin, S.M., Kelly, D., Patel, M.,
1080 Berthon, A., Syed, A., Yabe, M., et al. (2020). Cancer therapy shapes the fitness landscape
1081 of clonal hematopoiesis. Nature Genetics *52*, 1219-1226. 10.1038/s41588-020-00710-0.

1082 23. Coombs, C.C., Zehir, A., Devlin, S.M., Kishtagari, A., Syed, A., Jonsson, P., Hyman, D.M.,
1083 Solit, D.B., Robson, M.E., and Baselga, J. (2017). Therapy-related clonal hematopoiesis in
1084 patients with non-hematologic cancers is common and associated with adverse clinical
1085 outcomes. Cell stem cell *21*, 374-382. e374.

1086 24. Kleppe, M., Comen, E., Wen, H.Y., Bastian, L., Blum, B., Rapaport, F.T., Keller, M., Granot,
1087 Z., Socci, N., Viale, A., et al. (2015). Somatic mutations in leukocytes infiltrating primary
1088 breast cancers. npj Breast Cancer *1*, 15005. 10.1038/npjbcancer.2015.5.

1089 25. Severson, E.A., Riedlinger, G.M., Connelly, C.F., Vergilio, J.A., Goldfinger, M., Ramkissoon,
1090 S., Frampton, G.M., Ross, J.S., Fratella-Calabrese, A., Gay, L., et al. (2018). Detection of

1091 clonal hematopoiesis of indeterminate potential in clinical sequencing of solid tumor
1092 specimens. Blood *131*, 2501-2505. 10.1182/blood-2018-03-840629.

1093 26. Marshall, C.H., Gondek, L.P., Luo, J., and Antonarakis, E.S. (2022). Clonal Hematopoiesis of
1094 Indeterminate Potential in Patients with Solid Tumor Malignancies. Cancer Res *82*, 4107-
1095 4113. 10.1158/0008-5472.Can-22-0985.

1096 27. Pich, O., Bernard, E., Zagorulya, M., Rowan, A., Pospori, C., Slama, R., Huerga Encabo, H.,
1097 O'Sullivan, J., Papazoglou, D., Anastasiou, P., et al. (2025). Tumor-Infiltrating Clonal
1098 Hematopoiesis. New England Journal of Medicine *392*, 1594-1608.
1099 10.1056/NEJMoa2413361.

1100 28. Buttigieg, M.M., Vlasschaert, C., Bick, A.G., Vanner, R.J., and Rauh, M.J. (2025).
1101 Inflammatory reprogramming of the solid tumor microenvironment by infiltrating clonal
1102 hematopoiesis is associated with adverse outcomes. Cell Rep Med *6*, 101989.
1103 10.1016/j.xcrm.2025.101989.

1104 29. Pan, W., Zhu, S., Qu, K., Meeth, K., Cheng, J., He, K., Ma, H., Liao, Y., Wen, X., Roden, C., et
1105 al. (2017). The DNA Methylcytosine Dioxygenase Tet2 Sustains Immunosuppressive
1106 Function of Tumor-Infiltrating Myeloid Cells to Promote Melanoma Progression. Immunity
1107 *47*, 284-297.e285. https://doi.org/10.1016/j.immuni.2017.07.020.

1108 30. Nguyen, Y.T.M., Fujisawa, M., Nguyen, T.B., Suehara, Y., Sakamoto, T., Matsuoka, R., Abe,
1109 Y., Fukumoto, K., Hattori, K., Noguchi, M., et al. (2021). Tet2 deficiency in immune cells
1110 exacerbates tumor progression by increasing angiogenesis in a lung cancer model. Cancer
1111 Sci *112*, 4931-4943. 10.1111/cas.15165.

1112 31. Krishnan, T., Solar Vasconcelos, J.P., Titmuss, E., Topham, J.T., Schaeffer, D.F., Karsan, A.,
1113 Lim, H.J., Ho, C., Gill, S., Kennecke, H.F., et al. (2024). Clonal hematopoiesis of
1114 indeterminate potential (CHIP), treatment outcomes and adverse events in
1115 gastrointestinal cancers: A pooled analysis of clinical trial and real-world data. Journal of
1116 Clinical Oncology *42*, 169-169. 10.1200/JCO.2024.42.3_suppl.169.

1117 32. Reed, S.C., Croessmann, S., and Park, B.H. (2023). CHIP Happens: Clonal Hematopoiesis of
1118 Indeterminate Potential and Its Relationship to Solid Tumors. Clin Cancer Res *29*, 1403-
1119 1411. 10.1158/1078-0432.Ccr-22-2598.

1120 33. Rondeau, V., Bansal, S., Buttigieg, M.M., Zeng, A.G.X., Chan, D.Y., Chan-Seng-Yue, M., Jin,
1121 L., McLeod, J., Kates, M., Donato, E., et al. (2026). Response to Immune Checkpoint
1122 Blockade Is Enhanced in the Presence of Hematopoietic TET2 Inactivation. Cancer
1123 Research, OF845-OF857. 10.1158/0008-5472.CAN-24-3329.

1124 34. Nguyen, B., Fong, C., Luthra, A., Smith, S.A., DiNatale, R.G., Nandakumar, S., Walch, H.,
1125 Chatila, W.K., Madupuri, R., Kundra, R., et al. (2022). Genomic characterization of
1126 metastatic patterns from prospective clinical sequencing of 25,000 patients. Cell *185*, 563-
1127 575.e511. https://doi.org/10.1016/j.cell.2022.01.003.

1128 35. Quivoron, C., Couronne, L., Della Valle, V., Lopez, C.K., Plo, I., Wagner-Ballon, O., Do
1129 Cruzeiro, M., Delhommeau, F., Arnulf, B., Stern, M.H., et al. (2011). TET2 inactivation
1130 results in pleiotropic hematopoietic abnormalities in mouse and is a recurrent event
1131 during human lymphomagenesis. Cancer Cell *20*, 25-38. S1535-6108(11)00225-X [pii]

1132 10.1016/j.ccr.2011.06.003.

1133 36. Stadtfeld, M., and Graf, T. (2005). Assessing the role of hematopoietic plasticity for
1134 endothelial and hepatocyte development by non-invasive lineage tracing. Development
1135 *132*, 203-213. 10.1242/dev.01558.

1136 37. Lee, P.P., Fitzpatrick, D.R., Beard, C., Jessup, H.K., Lehar, S., Makar, K.W., Pérez-Melgosa,
1137 M., Sweetser, M.T., Schlissel, M.S., Nguyen, S., et al. (2001). A critical role for Dnmt1 and
1138 DNA methylation in T cell development, function, and survival. Immunity *15*, 763-774.
1139 10.1016/s1074-7613(01)00227-8.

1140 38. Rickert, R.C., Roes, J., and Rajewsky, K. (1997). B lymphocyte-specific, Cre-mediated
1141 mutagenesis in mice. Nucleic Acids Res *25*, 1317-1318. 10.1093/nar/25.6.1317.

1142 39. Clausen, B.E., Burkhardt, C., Reith, W., Renkawitz, R., and Forster, I. (1999). Conditional
1143 gene targeting in macrophages and granulocytes using LysMcre mice. Transgenic Res *8*,
1144 265-277. 10.1023/a:1008942828960.

1145 40. Nakayama, M., Hong, C.P., Oshima, H., Sakai, E., Kim, S.-J., and Oshima, M. (2020). Loss of
1146 wild-type p53 promotes mutant p53-driven metastasis through acquisition of survival and
1147 tumor-initiating properties. Nature Communications *11*, 2333. 10.1038/s41467-020-
1148 16245-1.

1149 41. Huang, D.W., Sherman, B.T., Tan, Q., Collins, J.R., Alvord, W.G., Roayaei, J., Stephens, R.,
1150 Baseler, M.W., Lane, H.C., and Lempicki, R.A. (2007). The DAVID Gene Functional
1151 Classification Tool: a novel biological module-centric algorithm to functionally analyze
1152 large gene lists. Genome Biology *8*, R183. 10.1186/gb-2007-8-9-r183.

1153 42. Subramanian, A., Tamayo, P., Mootha, V.K., Mukherjee, S., Ebert, B.L., Gillette, M.A.,
1154 Paulovich, A., Pomeroy, S.L., Golub, T.R., Lander, E.S., and Mesirov, J.P. (2005). Gene set
1155 enrichment analysis: a knowledge-based approach for interpreting genome-wide
1156 expression profiles. Proc Natl Acad Sci U S A *102*, 15545-15550. 0506580102 [pii]

1157 10.1073/pnas.0506580102.

1158 43. Godec, J., Tan, Y., Liberzon, A., Tamayo, P., Bhattacharya, S., Butte, A.J., Mesirov, J.P., and
1159 Haining, W.N. (2016). Compendium of Immune Signatures Identifies Conserved and
1160 Species-Specific Biology in Response to Inflammation. Immunity *44*, 194-206.
1161 10.1016/j.immuni.2015.12.006.

1162 44. Aibar, S., González-Blas, C.B., Moerman, T., Huynh-Thu, V.A., Imrichova, H., Hulselmans,
1163 G., Rambow, F., Marine, J.-C., Geurts, P., Aerts, J., et al. (2017). SCENIC: single-cell
1164 regulatory network inference and clustering. Nature Methods *14*, 1083-1086.
1165 10.1038/nmeth.4463.

1166 45. Zhang, C., Sheng, Q., Zhang, X., Xu, K., Jin, X., Zhou, W., Zhang, M., Lv, D., Yang, C., Li, Y., et
1167 al. (2023). Prioritizing exhausted T cell marker genes highlights immune subtypes in pan-
1168 cancer. iScience *26*, 106484. https://doi.org/10.1016/j.isci.2023.106484.

1169 46. Trapnell, C., Cacchiarelli, D., Grimsby, J., Pokharel, P., Li, S., Morse, M., Lennon, N.J., Livak,
1170 K.J., Mikkelsen, T.S., and Rinn, J.L. (2014). The dynamics and regulators of cell fate

1171 decisions are revealed by pseudotemporal ordering of single cells. Nature Biotechnology
1172 *32*, 381-386. 10.1038/nbt.2859.

1173 47. Borcherding, N., Bormann, N.L., and Kraus, G. (2020). scRepertoire: An R-based toolkit for
1174 single-cell immune receptor analysis. F1000Res *9*, 47. 10.12688/f1000research.22139.2.

1175 48. Bosco, N., Swee, L.K., Bénard, A., Ceredig, R., and Rolink, A. (2010). Auto-reconstitution of
1176 the T-cell compartment by radioresistant hematopoietic cells following lethal irradiation
1177 and bone marrow transplantation. Experimental Hematology *38*, 222-232.e222.
1178 https://doi.org/10.1016/j.exphem.2009.12.006.

1179 49. Busque, L., Patel, J.P., Figueroa, M.E., Vasanthakumar, A., Provost, S., Hamilou, Z., Mollica,
1180 L., Li, J., Viale, A., Heguy, A., et al. (2012). Recurrent somatic TET2 mutations in normal
1181 elderly individuals with clonal hematopoiesis. Nature Genetics *44*, 1179-1181.
1182 10.1038/ng.2413.

1183 50. Zehir, A., Benayed, R., Shah, R.H., Syed, A., Middha, S., Kim, H.R., Srinivasan, P., Gao, J.,
1184 Chakravarty, D., Devlin, S.M., et al. (2017). Mutational landscape of metastatic cancer
1185 revealed from prospective clinical sequencing of 10,000 patients. Nature Medicine *23*,
1186 703-713. 10.1038/nm.4333.

1187 51. Jaiswal, S. (2020). Clonal hematopoiesis and nonhematologic disorders. Blood *136*, 1606-
1188 1614. 10.1182/blood.2019000989.

1189 52. Fraietta, J.A., Nobles, C.L., Sammons, M.A., Lundh, S., Carty, S.A., Reich, T.J., Cogdill, A.P.,
1190 Morrissette, J.J.D., DeNizio, J.E., Reddy, S., et al. (2018). Disruption of TET2 promotes the
1191 therapeutic efficacy of CD19-targeted T cells. Nature *558*, 307-312. 10.1038/s41586-018-
1192 0178-z.

1193 53. Dimitri, A.J., Baxter, A.E., Chen, G.M., Hopkins, C.R., Rouin, G.T., Huang, H., Kong, W.,
1194 Holliday, C.H., Wiebking, V., Bartoszek, R., et al. (2024). TET2 regulates early and late
1195 transitions in exhausted CD8(+) T cell differentiation and limits CAR T cell function. Sci Adv
1196 *10*, eadp9371. 10.1126/sciadv.adp9371.

1197 54. Wang, Y., Sano, S., Yura, Y., Ke, Z., Sano, M., Oshima, K., Ogawa, H., Horitani, K., Min, K.D.,
1198 Miura-Yura, E., et al. (2020). Tet2-mediated clonal hematopoiesis in nonconditioned mice
1199 accelerates age-associated cardiac dysfunction. JCI Insight *5*. 10.1172/jci.insight.135204.

1200 55. Fuster, J.J., MacLauchlan, S., Zuriaga, M.A., Polackal, M.N., Ostriker, A.C., Chakraborty, R.,
1201 Wu, C.L., Sano, S., Muralidharan, S., Rius, C., et al. (2017). Clonal hematopoiesis associated
1202 with TET2 deficiency accelerates atherosclerosis development in mice. Science *355*, 842-
1203 847. 10.1126/science.aag1381.

1204 56. Jaiswal, S., Natarajan, P., Silver Alexander, J., Gibson Christopher, J., Bick Alexander, G.,
1205 Shvartz, E., McConkey, M., Gupta, N., Gabriel, S., Ardissino, D., et al. Clonal Hematopoiesis
1206 and Risk of Atherosclerotic Cardiovascular Disease. New England Journal of Medicine *377*,
1207 111-121. 10.1056/NEJMoa1701719.

1208 57. Sano, S., Oshima, K., Wang, Y., MacLauchlan, S., Katanasaka, Y., Sano, M., Zuriaga, M.A.,
1209 Yoshiyama, M., Goukassian, D., Cooper, M.A., et al. (2018). Tet2-Mediated Clonal

1210 Hematopoiesis Accelerates Heart Failure Through a Mechanism Involving the IL-
1211 1β/NLRP3 Inflammasome. J Am Coll Cardiol *71*, 875-886. 10.1016/j.jacc.2017.12.037.

1212 58. Bolton, K.L., Gillis, N.K., Coombs, C.C., Takahashi, K., Zehir, A., Bejar, R., Garcia-Manero, G.,
1213 Futreal, A., Jensen, B.C., Diaz, L.A., Jr., et al. (2019). Managing Clonal Hematopoiesis in
1214 Patients With Solid Tumors. J Clin Oncol *37*, 7-11. 10.1200/jco.18.00331.

1215 59. Li, S., Feng, J., Wu, F., Cai, J., Zhang, X., Wang, H., Fetahu, I.S., Iwanicki, I., Ma, D., Hu, T., et
1216 al. (2020). TET2 promotes anti-tumor immunity by governing G-MDSCs and CD8+ T-cell
1217 numbers. EMBO reports *21*, e49425. https://doi.org/10.15252/embr.201949425.

1218 60. Carty, S.A., Gohil, M., Banks, L.B., Cotton, R.M., Johnson, M.E., Stelekati, E., Wells, A.D.,
1219 Wherry, E.J., Koretzky, G.A., and Jordan, M.S. (2018). The Loss of TET2 Promotes CD8(+) T
1220 Cell Memory Differentiation. J Immunol *200*, 82-91. 10.4049/jimmunol.1700559.

1221 61. Yue, X., Trifari, S., Äijö, T., Tsagaratou, A., Pastor, W.A., Zepeda-Martínez, J.A., Lio, C.W., Li,
1222 X., Huang, Y., Vijayanand, P., et al. (2016). Control of Foxp3 stability through modulation of
1223 TET activity. J Exp Med *213*, 377-397. 10.1084/jem.20151438.

1224 62. Khan, O., Giles, J.R., McDonald, S., Manne, S., Ngiow, S.F., Patel, K.P., Werner, M.T., Huang,
1225 A.C., Alexander, K.A., Wu, J.E., et al. (2019). TOX transcriptionally and epigenetically
1226 programs CD8+ T cell exhaustion. Nature *571*, 211-218. 10.1038/s41586-019-1325-x.

1227 63. Kim, K., Park, S., Park, S.Y., Kim, G., Park, S.M., Cho, J.W., Kim, D.H., Park, Y.M., Koh, Y.W.,
1228 Kim, H.R., et al. (2020). Single-cell transcriptome analysis reveals TOX as a promoting
1229 factor for T cell exhaustion and a predictor for anti-PD-1 responses in human cancer.
1230 Genome Med *12*, 22. 10.1186/s13073-020-00722-9.

1231 64. Zhang, X., Wang, Y., Xue, H., Zhao, Y., Liu, M., Wei, H., and Liu, Q. (2025). Clonal
1232 hematopoiesis of indeterminate potential and risk of autoimmune thyroid disease. BMC
1233 Med *23*, 237. 10.1186/s12916-025-04077-z.

1234 65. Liu, Q., Wästerlid, T., Smedby, K.E., Xue, H., Boberg, E., Fang, F., and Liu, X. (2025). Clonal
1235 hematopoiesis of indeterminate potential and risk of immune thrombocytopenia. J Intern
1236 Med *297*, 672-682. 10.1111/joim.20092.

1237 66. Jaber Chehayeb, R., Singh, J., Matute-Martinez, C., Chen, N.W., Guajardo, A.F., Lin, D.,
1238 Jayakrishnan, R., Christofides, A., Leveille, E., Im, Y., et al. (2024). Clonal hematopoiesis of
1239 indeterminate potential is associated with increased risk of immune checkpoint inhibitor
1240 myocarditis in a prospective study of a cardio-oncology cohort. Cardiooncology *10*, 84.
1241 10.1186/s40959-024-00289-z.

1242 67. Gao, Q., Shen, K., and Xiao, M. (2024). TET2 mutation in acute myeloid leukemia: biology,
1243 clinical significance, and therapeutic insights. Clin Epigenetics *16*, 155. 10.1186/s13148-
1244 024-01771-2.

1245 68. An, J., González-Avalos, E., Chawla, A., Jeong, M., López-Moyado, I.F., Li, W., Goodell, M.A.,
1246 Chavez, L., Ko, M., and Rao, A. (2015). Acute loss of TET function results in aggressive
1247 myeloid cancer in mice. Nature Communications *6*, 10071. 10.1038/ncomms10071.

1248 69. Muto, H., Sakata-Yanagimoto, M., Nagae, G., Shiozawa, Y., Miyake, Y., Yoshida, K., Enami,
1249 T., Kamada, Y., Kato, T., Uchida, K., et al. (2014). Reduced TET2 function leads to T-cell

1250 lymphoma with follicular helper T-cell-like features in mice. Blood Cancer J *4*, e264.
1251 10.1038/bcj.2014.83.

1252 70. Vanner, R., Zeng, A.G.X., Chan-Seng-Yue, M., Bansal, S., Donato, E., Jin, L., Genta, S., Sanz
1253 Garcia, E., Chan, S.M., Trumpp, A., and Dick, J.E. (2023). Somatic TET2 Mutations Prime the
1254 Immune System for Response to Immune Checkpoint Blockade. Blood *142*, 2689-2689.
1255 10.1182/blood-2023-177740.

1256 71. Carty, S.A., Gohil, M., Koretzky, G.A., and Jordan, M.S. (2014). TET2 Regulates CD8+ T Cell
1257 Differentiation. Blood *124*, 1423-1423. 10.1182/blood.V124.21.1423.1423.

1258 72. Sakai, E., Nakayama, M., Oshima, H., Kouyama, Y., Niida, A., Fujii, S., Ochiai, A., Nakayama,
1259 K.I., Mimori, K., Suzuki, Y., et al. (2018). Combined Mutation of Apc, Kras, and Tgfbr2
1260 Effectively Drives Metastasis of Intestinal Cancer. Cancer Research *78*, 1334-1346.
1261 10.1158/0008-5472.CAN-17-3303.

1262 73. Fujisawa, M., Nguyen, T.B., Abe, Y., Suehara, Y., Fukumoto, K., Suma, S., Makishima, K.,
1263 Kaneko, C., Nguyen, Y.T.M., Usuki, K., et al. (2022). Clonal germinal center B cells function
1264 as a niche for T-cell lymphoma. Blood *140*, 1937-1950. 10.1182/blood.2022015451.

1265 74. Krämer, A., Green, J., Pollard, J., Jr., and Tugendreich, S. (2014). Causal analysis approaches
1266 in Ingenuity Pathway Analysis. Bioinformatics *30*, 523-530. 10.1093/bioinformatics/btt703.

1267 75. Hao, Y., Stuart, T., Kowalski, M.H., Choudhary, S., Hoffman, P., Hartman, A., Srivastava, A.,
1268 Molla, G., Madad, S., Fernandez-Granda, C., and Satija, R. (2024). Dictionary learning for
1269 integrative, multimodal and scalable single-cell analysis. Nature Biotechnology *42*, 293-
1270 304. 10.1038/s41587-023-01767-y.

1271 76. Germain, P.L., Lun, A., Garcia Meixide, C., Macnair, W., and Robinson, M.D. (2021).
1272 Doublet identification in single-cell sequencing data using scDblFinder. F1000Res *10*, 979.
1273 10.12688/f1000research.73600.2.

1274 77. Venturi, V., Kedzierska, K., Turner, S.J., Doherty, P.C., and Davenport, M.P. (2007).
1275 Methods for comparing the diversity of samples of the T cell receptor repertoire. J
1276 Immunol Methods *321*, 182-195. 10.1016/j.jim.2007.01.019.

1277 78. Thomas, P.G., Handel, A., Doherty, P.C., and La Gruta, N.L. (2013). Ecological analysis of
1278 antigen-specific CTL repertoires defines the relationship between naïve and immune T-cell
1279 populations. Proceedings of the National Academy of Sciences *110*, 1839-1844.
1280 10.1073/pnas.1222149110.

1281 79. Greiff, V., Bhat, P., Cook, S.C., Menzel, U., Kang, W., and Reddy, S.T. (2015). A
1282 bioinformatic framework for immune repertoire diversity profiling enables detection of
1283 immunological status. Genome Medicine *7*, 49. 10.1186/s13073-015-0169-8.

1284 80. Miura, F., Shibata, Y., Miura, M., Sangatsuda, Y., Hisano, O., Araki, H., and Ito, T. (2019).
1285 Highly efficient single-stranded DNA ligation technique improves low-input whole-genome
1286 bisulfite sequencing by post-bisulfite adaptor tagging. Nucleic Acids Research *47*, e85-e85.
1287 10.1093/nar/gkz435.

1288 81. Miura, F., Shibata, Y., Miura, M., Inatomi, K., Suzuki, Y., and Ito, T. (2025). Identification of
1289 an enzyme with strong single-stranded DNA ligation activity and its application for
1290 sequencing. Nucleic Acids Research *53*, gkaf054. 10.1093/nar/gkaf054.

1291 82. Krueger, F., and Andrews, S.R. (2011). Bismark: a flexible aligner and methylation caller for
1292 Bisulfite-Seq applications. Bioinformatics *27*, 1571-1572. 10.1093/bioinformatics/btr167.

1293